nature astronomy

Article

https://doi.org/10.1038/s41550-022-01844-3

Direct measurement of decimetre-sized rocky material in the Oort cloud

Received: 27 September 2021

Accepted: 26 October 2022

Published online: 12 December 2022

Check for updates

Denis Vida[1] ✉, Peter G. Brown[1], Hadrien A. R. Devillepoix[2], Paul Wiegert[1], Danielle E. Moser[3], Pavol Matlovič[4], Christopher D. K. Herd[5], Patrick J. A. Hill[5], Eleanor K. Sansom[2], Martin C. Towner[2], Juraj Tóth[4], William J. Cooke[6] & Donald W. Hladiuk[7]

The Oort cloud is thought to be a reservoir of icy planetesimals and the source of long-period comets (LPCs) implanted from the outer Solar System during the time of giant-planet formation. The abundance of rocky ice-free bodies is a key diagnostic of Solar System formation models as it can distinguish between 'massive' and 'depleted' proto-asteroid-belt scenarios and thus disentangle competing planet formation models. Here we report a direct observation of a decimetre-sized (~2 kg) rocky meteoroid on a retrograde LPC orbit (eccentricity ~1.0, inclination 121°). During its flight, it fragmented at dynamic pressures similar to fireballs dropping ordinary chondrite meteorites. A numerical ablation model fit produces bulk density and ablation properties also consistent with asteroidal meteoroids. We estimate the flux of rocky objects impacting Earth from the Oort cloud to be $1.08^{+2.81}_{-0.95}$ meteoroids per 10^6 km^2 yr^{-1} to a mass limit of 10 g. This corresponds to an abundance of rocky meteoroids of $\sim 6^{+13}_{-5}$% of all objects originating in the Oort cloud and impacting Earth to these masses. Our result gives support to migration-based dynamical models of the formation of the Solar System, which predict that significant rocky material is implanted in the Oort cloud, a result not explained by traditional Solar System formation models.

The sharp increase in the number of ground-based networks utilizing digital cameras for observing fireballs[1–5] in recent years has resulted in near-continuous coverage of almost 2% of Earth's atmosphere for small impactors. Supplementing these ground-based instruments in fireball detection is the Geostationary Lightning Mapper (GLM) instrument onboard the Geostationary Operational Environmental Satellite-16 (GOES-16) and GEOS-17. First deployed in 2016, the GLM now observes a total of ~1/3 of Earth's surface with a resolution of ~10 km at 500 frames per second in a narrow 1.1 nm pass band centred around the O I oxygen triplet at 777.4 nm (ref. [6]). The GLM is very efficient at detecting bright fireballs, which usually saturate ground-based cameras[7]. As camera saturation prevents an accurate estimate of meteoroid properties during atmospheric entry, the GLM extends the usable measurement size range of bolides compared with ground-based cameras. The larger ground-based camera coverage, which provides observations of fireball trajectories and orbits when fused with space-based light curves, records larger numbers of the decimetre-sized meteoroid population than previously possible and allows accurate estimates of their physical properties.

Observations from earlier fireball networks[8,9] have established that decimetre-sized chondritic-like meteoroids that penetrate deeper into the atmosphere predominantly come from asteroidal low-inclination

[1]Department of Physics and Astronomy, University of Western Ontario, London, Ontario, Canada. [2]Space Science and Technology Centre, Curtin University, Perth, Western Australia, Australia. [3]Jacobs ESSCA Group, NASA Marshall Space Flight Center, Huntsville, AL, USA. [4]Faculty of Mathematics, Physics and Informatics, Comenius University, Bratislava, Slovakia. [5]Department of Earth and Atmospheric Sciences, University of Alberta, Edmonton, Alberta, Canada. [6]NASA MEO, NASA Marshall Space Flight Center, Huntsville, AL, USA. [7]RASC Calgary Centre, Calgary, Alberta, Canada. ✉e-mail: denis.vida@gmail.com

https://doi.org/10.1038/s41550-022-01844-3

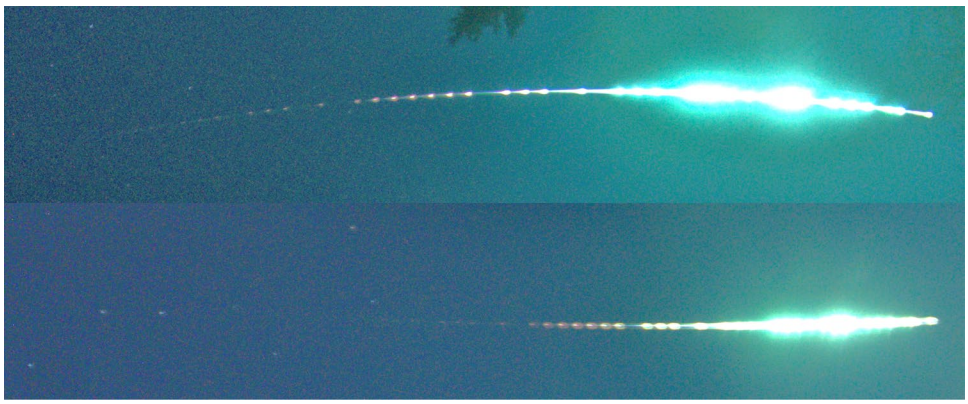

Fig. 1 | The fireball as seen from the two GFO stations. It was observed for a total of 2.4 s with a path length of 148.5 km. Top: Miquelon Lake. Bottom: Vermilion (the Big Dipper can be seen on the left side). The fireball is moving left to right, and the periodic breaks in the fireball are used to encode the absolute time to an accuracy of 1 ms.

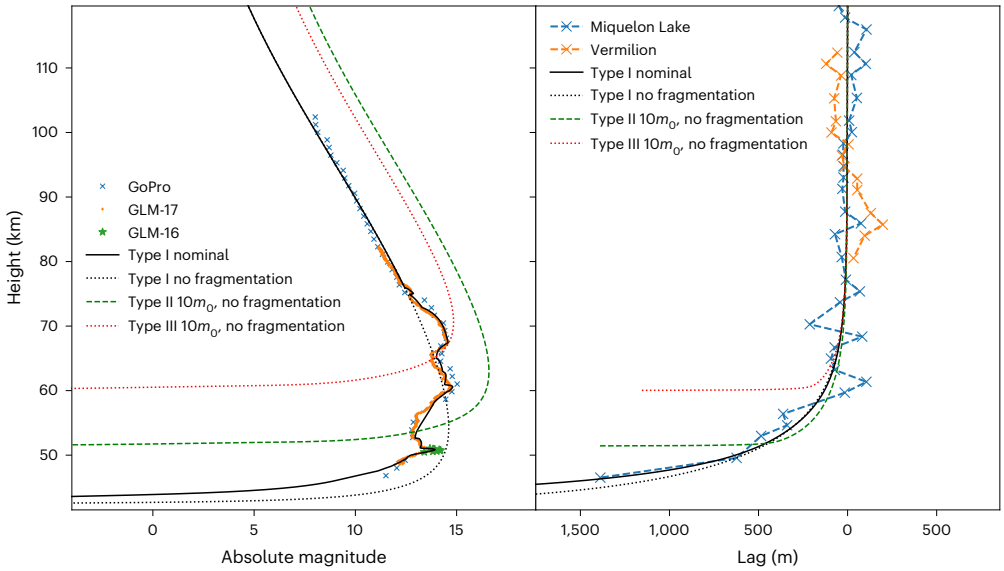

Fig. 2 | Observed and simulated light curve and deceleration profile. Left: observed and simulated light curve. The solid black line is the nominal fit with the parameters and fragmentation behaviour given in Supplementary Tables 6 and 7. A no-fragmentation solution for type I (black), type II (green) and type III (red) objects is also shown. The GLM light curve was calibrated to an accuracy of ±0.1 mag using three independent high-speed fireballs where GLM light curves and ground-based records were available. The GoPro light curve was calibrated to an accuracy of ±0.3 mag. Right: observed and simulated deceleration profile (lag) for various simulation scenarios. The lag is the distance a decelerating meteoroid falls behind a hypothetical non-decelerating meteoroid moving at the initially observed velocity. As the fireball showed a wake, it was not possible to determine the along-the-trajectory positions of the leading fragment to the same accuracy as the transverse positions. The lag measurement errors are reflected in the scatter around the zero lag axis, which is on the order of ±200 m. The Cochrane security camera was not used for velocity measurement due to lower accuracy.

orbits. Similarly, most friable meteoroids that disrupt high in the atmosphere were measured to be on Jupiter-family comet (JFC), Halley-type comet (HTC) or long-period comet (LPC) orbits[10]. Minor cross-contamination of material between asteroidal and JFC orbits is observed and can be explained by their dynamical evolution[11], consistent with telescopic observations of comets and asteroids[12]. In situ measurements have found rocky (refractory) materials in comets[13], but these are small, microscopic chondrules and fragments of calcium–aluminium-rich inclusions, presumed to be embedded during comet formation. However, the presence of macroscopic (decimetre-sized) rocky material originating from the Oort cloud (HTCs and LPCs) is much harder to explain. The abundance in the Oort cloud of larger, refractory material that probably formed in the inner Solar System would be a key diagnostic in distinguishing between dynamical models of early Solar System formation[14–16].

Contemporary models that account for planetesimal collisions predict that a significant number of rocky objects can only be implanted in the Oort cloud during a Grand Tack dynamical instability episode caused by the radial migration of the giant planets early in Solar System history[17]. The dynamical instability causes removal of 50–90% of rocky material in what is now the asteroid belt in such a way as to reproduce the main belt's observed orbital and compositional distribution[18,19]. These migration models necessitate a 'massive' proto-asteroid belt scenario and predict the ratio of icy to rocky planetesimals in the Oort cloud to be between 100:1 and 2,000:1 (refs. [14–17,20–22]). Following this early and fast migration, a slower dynamical diffusion process is postulated to further remove ~70% of the main belt, leaving the mass we see today[23,24]. Recent studies have shown that to match the dynamical and geochemical evidence, the instability occurs as early as 30–60 Myr after the dissipation of gas in the protoplanetary disk[25–27].

The competing model of early Solar System formation, the pebble-accretion model[28], eschews the migration scenario but allows for the rapid formation of the giant planets before the solar gas nebula dissipates[29]. In the pebble-accretion model, filaments of millimetre- to

https://doi.org/10.1038/s41550-022-01844-3

centimetre-sized pebbles gravitationally collapse quickly to form planetesimals[30]. The planetesimals in the terrestrial region grow more efficiently than those beyond 1 au, so there is no requirement to scatter rocky material to explain the small masses of Mars and the asteroid belt[31]. As the initial mass of the proto-asteroid belt is assumed to be small, the pebble-accretion model predicts that virtually no scattered rocky objects are implanted into the Oort cloud. It predicts an icy/rocky ratio of at least 10,000:1 (ref. [16]).

The initial size of the proto-asteroid belt remains a contentious topic. Recent work[32] has suggested that the asteroid belt could have initially been empty and later populated separately by S- and C-type objects. In this model, S-type asteroids are implanted through simple gravitational diffusion as by-products of terrestrial planet formation with C-types implanted during the growth of the giant planets through aerodynamic drag destabilization[33]. This scenario is also compatible with an early onset of dynamical instability and migration of the giant planets, which seems to be a necessary element in the reproduction of observational constraints[34].

Recently, it has been shown that the migration-induced dynamical instability is also compatible with an enhanced version of the pebble-accretion model, which uses realistic opacities[35]. In this model, the terrestrial planets form fast in only ~10 Myr, and then planet migration is invoked as one of the possibilities to explain the hafnium–tungsten anomaly in Earth's mantle caused by the Theia impact[36]. Nevertheless, even though the 1.5 au to 4 au region is assumed to be a divergence zone[37] (in between the terrestrial and giant-planet convergence zones where growth occurs), planetesimals in the divergence zone only slowly dissipate into neighbouring regions and are not scattered into highly excited orbits.

The earliest evidence of macroscopic asteroidal material in the Oort cloud was the discovery of asteroid 1996 PW[14]. Despite its highly eccentric orbit (eccentricity $e = 0.9907$, inclination $i = 30.09°$, semi-major axis $a = 269.5$ au, period $p = 4{,}424$ yr, solution date 14 April 2021; https://ssd.jpl.nasa.gov/tools/sbdb_lookup.html#/?sstr=1996%20PW), it showed no cometary-like activity. It had a D-type asteroid reflectance spectrum[38–40], also similar to bare cometary nuclei observed at large solar distances; hence, its origin as asteroid or an extinct cometary nucleus was uncertain.

More such tailless-comet 'Manx' objects[41] have since been discovered, having a wide variety of surface properties, including S-type spectra consistent with anhydrous rocky material[42,43]. For example, comet C/2014 S3 (PANSTARRS) has an S-type reflectance spectrum; however, it shows activity consistent with sublimation of water ice[16]. To explain the discovery of Oort cloud S-type objects in the context of the Solar System formation models, dynamical simulations of the evolution of the distribution of cometary and asteroidal objects were performed by ref. [17]. Taking the collisional evolution of asteroids into account, they found that the Grand Tack model[18] is the only model that predicts a sufficient icy/rocky mass ratio of Oort cloud objects (on the order of 100:1) to explain the detection of the comet C/2014 S3.

The Panoramic Survey Telescope and Rapid Response System (Pan-STARRS1) observations of LPCs have found that there is a deficit of objects with diameters $D \lesssim 1$ km (ref. [44]), assuming the physical processes producing cometary activity are size independent. These data show a significant change in the cumulative size-frequency distribution (SFD) coefficient α, where $N_{\mathrm{cum}} \propto D^{-\alpha}$, for $D \approx 2.8$ km, with $\alpha = 3.6$ for larger, and $\alpha = 0.5$ for smaller objects, consistent with comet formation models[45]. Pan-STARRS1 is able to detect LPC objects down to a size of $D \approx 100$ m (ref. [44]). This means that either the small objects are devoid of volatiles or they do not exist.

As telescopic measurements of an object in an LPC orbit may be compromised by space weathering[46,47], a more direct way to probe bulk physical properties of LPC material is desirable. One alternative method is to observe fireballs associated with an LPC-type meteoroid entering the atmosphere[48,49]. Nevertheless, such observations suffer from small atmospheric collection areas, so detection of decimetre-sized objects on LPC orbits is rare[50].

Table 1 | Geocentric radiant and heliocentric orbit (J2000.0)

Description		Nominal value	95% Confidence interval	
			Lower	Upper
Geocentric right ascension of radiant (°)	α_g	271.922	271.856	271.990
Geocentric declination of radiant (°)	δ_g	+4.40	+4.19	+4.64
Geocentric velocity ($km\,s^{-1}$)	v_g	60.97	60.89	61.00
Semi-major axis (au)	a	104	50	230
Eccentricity	e	0.9941	0.9878	0.9973
Perihelion distance (au)	q	0.6150	0.6126	0.6170
Argument of perihelion (°)	ω	103.95	103.51	104.25
Longitude of ascending node (°)	Ω	333.857472	333.857460	333.857485
Inclination (°)	i	121.40	120.98	121.80
Aphelion distance (au)	Q	207	100	459
Period (yr)	T	1,059	357	3,484
Last perihelion date		2021-01-16.23	2021-01-16.06	2021-01-16.33
Tisserand parameter with respect to Jupiter	T_J	−0.46	−0.48	−0.40

By using the observed light curves and dynamics of millmetre- and centimetre-sized cometary meteoroids, their ablation behaviour is well explained if they are modelled as a highly porous (~90%) collection of 10–300-μm-sized silicate grains[51,52]. The grain size distribution derived from observations of cometary meteoroids matches well to in situ measurements of the JFC comet 67P/Churyumov–Gerasimenko[10,53]. Similarly, observations of decimetre-sized meteorite-dropping fireballs can be well explained by modelling them as rocky objects that fragment deep in the atmosphere when aerodynamic loading exceeds their global mechanical strength[54]. In most cases, global strengths of meteorite-producing fireballs are found to be much lower than the compressive strengths of their associated meteorites, a finding ascribed to internal cracks[49].

Categorizing meteoroid strength relies on a relative comparison of atmospheric ablation behaviour. Generally speaking, slower, more massive and stronger meteoroids penetrate deeper into the atmosphere. The PE criterion[48] removes the speed and mass bias so that the strength can be directly compared among observed meteoroids (Methods). Meteoroids can be sorted into several groups based on material strength: type I fireballs with $PE > -4.6$ are related to ordinary chondrites (strongest material), type II with $-5.25 \le PE \le -4.6$ are related to carbonaceous chondrites, and type III with $PE < -5.25$ are cometary (weakest material).

The first observation of a multi-centimetre-sized rocky meteoroid on an HTC orbit was recorded in 1997 over the Czech Republic, called the Karlštejn fireball[55,56]. The ~30 g object was on a retrograde orbit, $a = 3.5$ au, $i = 138°$, $e = 0.7$ and Tisserand's parameter with respect to Jupiter $T_J = 0.62$ (where $T_J > 3$ are asteroidal orbits, $2 < T_J < 3$ are short-period-comet orbits and $T_J < 2$ are LPC orbits). It entered the atmosphere at 65 km s^{-1} and penetrated down to an end height of 65 km, about 25 km deeper than cometary objects of similar speed and mass. It was classified as a type I (rocky) fireball based on its PE

https://doi.org/10.1038/s41550-022-01844-3

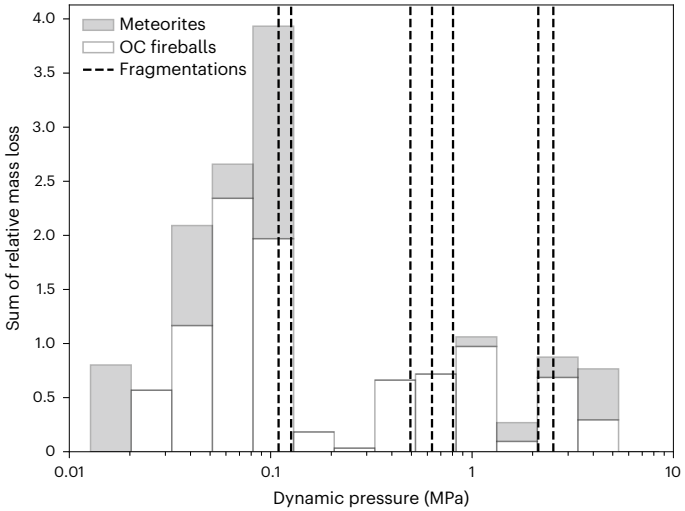

Fig. 3 | Observed fragmentations of the Alberta meteoroid compared with previously observed fragmentation behaviour of OC fireballs. The dynamic pressure ($\Gamma\rho_{air}v^2$) is computed using the drag coefficient of $\Gamma = 1.0$ to be consistent with values from ref. [49]. The uncertainty in the dynamic pressure due to short-term variations in the air mass density that are not captured by the NRLMSISE-00 model[83] is about 25%. However, uncertainties due to the unknown values of Γ in the flow regime of this meteoroid are not quantified. The vertical dashed lines indicate observed fragmentations of the Alberta meteoroid. The grey bars show the sum of relative mass loss at the given dynamic pressure for fireballs with recovered meteorites, and white bars are for (OC) fireballs with currently unrecovered meteorites, or which were too small to produce meteorites.

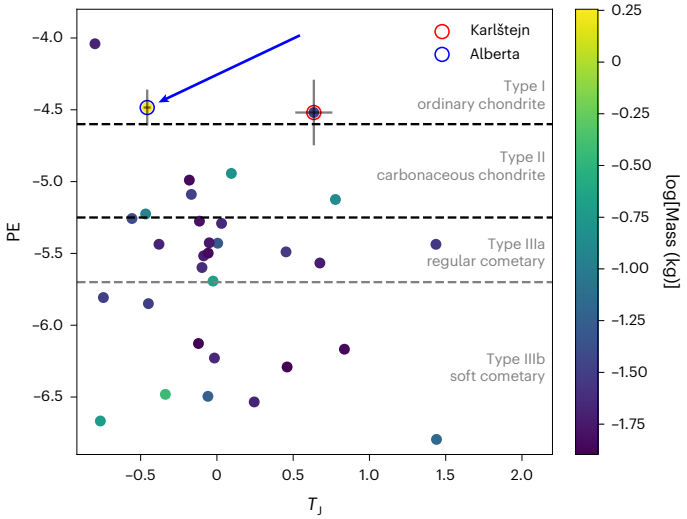

Fig. 4 | All published fireball data showing PE as a function of T_J for $T_J < 2$ fireballs in the MORP dataset. PE is a meteoroid strength factor (see Methods for more details). The type I (rocky) objects of interest above the PE = −4.6 dividing line between type I/II fireballs form a clearly separate grouping. The blue arrow points to the Alberta event. The MORP dataset does not contain formal uncertainties, but they are of the same order as for the Alberta event.

value. Its spectrum was highly depleted in volatile elements, notably sodium, and distinct from cometary fireballs. It reached a maximum dynamic pressure ($P_{dyn} = v^2\rho_{air}$, where v is the velocity and ρ_{air} is the air mass density) of 660 kPa before ablating away gradually, indicating that the true mechanical strength of the body was not reached as there was no evidence of catastrophic disruption. The dynamics of the body were consistent with a bulk density of 3,700 kg m^{-3}. Nevertheless, the semi-major axis was smaller than most LPCs and the dynamic pressures were lower than what decimetre-sized chondritic meteorite-dropping fireballs survive, probably due to the small mass of the body. The authors theorized that it was a centimetre-sized rocky component originally embedded in a comet, perhaps as part of an irradiated crust[55].

Records from decades of meteor-shower observations have not revealed any macroscopic (>centimetre-sized) lithic material mixed in with fragile HTC or LPC meteoroids. Smaller inclusions have been documented, notably several millimetre-sized type I fragments of Leonid fireballs were observed during the 1998 Leonid fireball storm[57–59] as have some gram-sized type I Taurids[1]. However, the Taurids are an unusual stream; they are on the dynamical boundary between JFC and asteroidal orbits, are generally classified as type II material, can be difficult to separate from the sporadic background, and have an origin probably related to fragmentation rather than gas drag sublimation[60].

Results

Here we report the direct observation of a decimetre-sized rocky meteoroid (PE = −4.49, type I) on an LPC orbit ($i = 121°$, $e \approx 1.0$, $T_J = -0.46$; Table 1). This meteoroid reached dynamic pressures similar to those of ordinary chondrites. The ~2 kg body entered the atmosphere ~100 km north of Edmonton, Alberta, Canada on 22 February 2021 at 13:23:17 UTC. Its full atmospheric luminous path was recorded by two Global Fireball Observatory (GFO) all-sky cameras[3] (Fig. 1) and over 200 security and dash cameras. In addition, it was detected by the GLM instruments onboard the GOES-16 and GOES-17 satellites, permitting measurement of its unsaturated light curve (see 'Photometric calibration' in Supplementary Information). We used the most recent astrometric calibration methods[5] and computed the atmospheric trajectory (internal accuracy of 30 m) using the GFO data and using one additional security camera (accuracy 70 m) (see 'Astrometric calibration' in Supplementary Information). The fireball entered the atmosphere with a velocity of 62.1 km s^{-1} and penetrated down to a height of 46.5 km, about 20 km deeper than the Karlštejn event that had a similar velocity but a 70× smaller mass. The parent body search did not return any matches, an expected result given the large orbital period.

Ablation modelling

The dynamics, light curve and the fragmentation behaviour were modelled using a semi-empirical meteoroid ablation model[54] (Methods) that has been successfully applied to multiple meteorite-producing fireballs, as well as cometary meteoroids. The comparison between observations and the model fit is shown in Fig. 2; the modelling details are given in 'Modelling results' in Supplementary Information. A bulk density of $\rho_m = 3{,}300$ kg m^{-3}, as appropriate for chondritic meteorite-dropping fireballs[9], fits the observed dynamics well.

As a demonstration of how improbable that this was a weak, cometary-like body, we modelled a non-fragmenting fireball using physical properties appropriate for cometary meteoroids (ablation coefficient $\sigma = 0.08$ kg MJ^{-1}, $\rho_m = 1{,}000$ k gm^{-3} and luminous efficiency τ for type III bodies[61,62]), with a 10× larger pre-atmospheric mass (20 kg) than the Alberta fireball keeping the same trajectory parameters. The hypothetical cometary meteoroid only penetrated down to a height of ~60 km.

The simulation was repeated for a hypothetical carbonaceous-chondrite meteoroid ($\sigma = 0.042$ kg MJ^{-1}, $\rho_m = 2{,}000$ kg m^{-3}, τ for type II bodies[61,62]) with the same 20 kg mass. In this case, the meteoroid only penetrated to a height of 53 km while the simulated light curve was ~2.5 magnitudes brighter than observed.

We found no combination of model parameters for carbonaceous-chondrite or cometary-like material that could fit the observations. If these hypothetical type II and type III objects had the same mass as our type I rocky object, their end heights would have been a further 8 km higher than these values. From other fireball measurements, a cometary body at these speeds and masses is not expected to withstand the aerodynamic loading below ~80 km without fragmenting[60].

https://doi.org/10.1038/s41550-022-01844-3

Table 2 | All T_J < 2 type I objects in the literature satisfying our criteria

Name	PE	T_J	Mass (kg)	a (au)	q (au)	e	i (°)	ω (°)	Ω (°)
Alberta (this work)	$-4.49^{+0.12}_{-0.13}$	$-0.46^{+0.06}_{-0.02}$	$1.8^{+1.8}_{-0.9}$	104^{+126}_{-54}	$0.615^{+0.002}_{-0.002}$	$0.994^{+0.003}_{-0.006}$	$121.40^{+0.4}_{-0.4}$	$104.0^{+0.3}_{-0.4}$	333.86
Karlštejn[55]	$-4.53^{+0.42}_{-0.23}$	$0.64^{+0.12}_{-0.18}$	$0.033^{+0.082}_{-0.030}$	$3.5^{+0.18}_{-0.18}$	$1.012^{+0.0002}_{-0.0002}$	$0.710^{+0.016}_{-0.016}$	$137.90^{+0.10}_{-0.10}$	$174.60^{+0.14}_{-0.14}$	71.55
MORP 441[63]	−4.04	−0.78	0.020	24.7	0.765	0.969	159.7	56.7	103.8

The errors for Karlštejn and the Alberta event are the 95% confidence intervals. We assumed a conservative uncertainty in the mass of the Alberta event of a factor of 2, due to possible variations in the luminous efficiency[106]. Karlštejn has larger uncertainties as the mass was only derived dynamically (0.003 kg to 0.1 kg), which we converted to the contemporary mass scale (from ref. [48] to ref. [49]). The orbital uncertainties for the Karlštejn fireball are symmetric and taken from the original publication[55]. The MORP dataset does not contain any uncertainties. The uncertainty of the ascending node is near zero as it reflects the time of the meteoroid intersecting Earth's orbit (that is, entering the atmosphere), which is accurately known. However for MORP, the uncertainty in the timing for some fireballs is on the order of tens of minutes ($\pm 10^{-5}$° in the ascending node).

The fireball fragmented under dynamic pressures similar to those observed for rocky meteoroids. Reference [49] analysed the fragmentation behaviour of several instrumentally observed ordinary chondrite (OC) meteorite-dropping fireballs. They found that OC meteoroids do not fragment randomly but follow a specific pattern. The first phase of fragmentations occurs at dynamic pressures between 0.04 MPa and 0.12 MPa, interpreted as being caused by detaching of weakly cemented fragments from the surface. The second phase occurs between 0.5 MPa and 5 MPa, presumably due to weaknesses associated with internal cracks.

Figure 3 shows their measurements of relative fragmentation mass loss versus the dynamic pressure for a collection of fireballs with recovered OC meteorites and fireballs of OC physical properties that were too small to produce meteorites. The dynamic pressure at fragmentation measured for the Alberta fireball matches well to the chondritic fragmentation profile.

Flux of rocky meteoroids from the Oort cloud

It is possible to estimate the flux and the ratio of type I (rocky) objects compared with weaker type II/III from the Oort cloud at the limiting mass appropriate for fast fireballs. The only published source for which there are reliable mass and time–area product estimates is the fireball dataset of the Meteorite Observation and Recovery Project (MORP)[63]. MORP is the only unbiased 'clear sky' survey of fireballs. There are a total of 30 fireballs with $T_J < 2$, speed > 50 km s^{-1} and a mass larger than 10 g in the MORP dataset. The speed limit removes the speed-dependent mass sensitivity[61], allowing us to set a consistent limiting mass for the flux. We set the mass limit to 10 g (in the contemporary mass scale following ref. [49]), for which the dataset is complete. This mass is also significantly larger than any previously observed refractory inclusions in cometary material; the largest type I Taurids are an order of magnitude smaller[1].

Among the population of 30 fireballs with $T_J < 2$, only one is a type I object (MORP catalogue number 441 with $m = 20$ g), which was also on a retrograde orbit ($e = 0.969$, $i = 159.7°$). This additional fireball, together with Karlštejn and the Alberta event, forms an isolated group among all published fireballs: they have $T_J < 1$, retrograde orbits, and are quite far from the PE dividing line for type II objects (Fig. 4 and Table 2).

The total time–area product for the MORP clear-sky survey was 1.51×10^{10} km^2 h (ref. [63]). Given the 29 MORP fireballs satisfying our orbital criteria, the total flux of carbonaceous and cometary (type II and III) objects can be computed. Assuming that times of meteor events are distributed according to the Poisson distribution[64], the 95% confidence interval is computed using the exact method[65] as [Pr(α/2, 2x), Pr(1 − α/2, 2(x + 1))], where Pr is the percent point function of the χ^2 distribution, $x = 29$ is the number of observed events and $\alpha = 0.05$ (that is, the 95% confidence interval). The corresponding range of observed events is [19.4, 41.7], producing a flux of $16.8^{+7.3}_{-5.6}$ meteoroids per 10^6 km^2 yr^{-1} to a mass limit of 10 g.

As a check on the flux values and ranges we derive, we use data from the GFO cameras in Alberta. These were gradually deployed starting with three cameras in July 2018, completing deployment with five cameras in November 2018. We used known deployment times and atmospheric coverage to compute a time series of common collecting area for the network; 0.24×10^6 km^2 for the three-camera configuration and 0.45×10^6 km^2 for the five-camera configuration. The common area was computed as an intersection of at least two camera fields of view at a height of 70 km and within a radius of 300 km from an individual camera[3]. Given that the average daily effective collection time is 3 h per day in Alberta[66], we estimate that the time–area product for the network up until February 2021 is 1.2×10^9 km^2 h. This network has yet to record a single type II or type III object on an LPC orbit in that time period, although it should have observed approximately two given the MORP flux. Using Poisson statistics, the probability for this non-observation is 10%, which is within statistical significance.

The total time–area product for $T_J < 2$ rocky type I events is 1.63×10^{10} km^2 h, derived by combining the values from the two networks. Note that the product is entirely dominated by the MORP survey, making up 90% of the total. We only include the Alberta event and the MORP 441 fireball in the flux estimate. To include the Karlštejn fireball, we would need an accurate estimate of the completeness and the time–area product for the contemporary European network[66], which is not available.

Given that only two events were observed, the 95% Poisson confidence interval is [0.24, 7.22] for the number of events. The total flux of rocky type I objects on LPC orbits is thus $1.08^{+2.81}_{-0.95}$ meteoroids per 10^6 km^2 yr^{-1} for a mass limit of 10 g, or $6.0^{+12.8}_{-5.2}$% of the total flux of all meteoroids impacting Earth on LPC orbits. This suggests of order 1–20% (about 1 in 5 to about 1 in 100) of LPC meteoroids at tens of grams sizes or larger are rocky.

Discussion

The confirmation of the existence and a comparatively high abundance of macroscopic lithic objects in the Oort cloud, constraining the ratio of icy/rocky objects to between 130:1 and 5:1 for masses >10 g (95% confidence interval), supports the need for a mechanism of ejection of inner Solar System material into nearly hyperbolic orbits. Even in a scenario where most of the Oort cloud objects are captured from other star systems[67], an ejection mechanism still needs to be present to explain the radial mixing of material.

We interpret the icy/rocky ratio as an intrinsic parameter of the population, assuming that it has remained unchanged in the Oort cloud since its implantation during the formation of the Solar System, as it is consistent with reflectance spectra surveys of large Oort cloud objects[17], which predict an icy/rocky ratio on the order of 100:1.

Was the Alberta fireball itself a primordial object? Collisions between similarly sized Oort cloud objects are very rare across the range of sizes[68,69]; however, >100 m bodies are known to experience surface processing due to impacts of metre-sized and smaller objects. Surface gardening and erosion due to micrometre-sized dust impacts from the interstellar medium[70] is generally experienced by objects of all sizes. The interstellar-medium erosion model predicts that all primordial objects smaller than a few metres should have been eroded away[71], indicating that the Alberta fireball possibly originated from a larger parent asteroid.

Our findings support a massive proto-asteroid-belt scenario as the source of rocky objects. Recent work[17] has shown that the Grand Tack dynamical instability model is the only one able to reproduce the observed abundance of rocky material in the Oort cloud, predicting that the total icy/rocky ratio depends on the duration of the instability. As the model predicts more rocky material is implanted if the instability occurs faster, direct measurement of the icy/rocky fraction can be used to constrain the duration of the early instability. These findings challenge Solar System formation models based on pebble accretion alone, which currently cannot explain the high observed abundance of rocky material in the Oort cloud as derived from fireball measurements and telescopic reflectance spectra data.

Methods

Ablation and fragmentation model

The dynamics and light curve of the fireball were simulated using the established semi-empirical model[54] that has been successfully applied to reconstruct the fragmentation behaviour and physical properties of many meteorite-dropping fireballs[49,72–74] and fainter meteors[10,51]. In this model, the meteoroid is initially treated as a single body, but increases in brightness and sudden deceleration are explained by fragmentation. Previous studies established several main modes of fragmentation: splitting into several single-body fragments, steady erosion of 10-µm- to 1-mm-sized refractory constituent grains from the meteoroid's surface, ejection of an eroding fragment and a sudden release of dust (that is, a large number of constituent grains)[54].

All fragments and grains are modelled using the classical equations of single-body ablation[61]:

$$\frac{\mathrm{d}v}{\mathrm{d}t} = -Km^{-1/3}\rho_{\mathrm{air}}v^2, \tag{1}$$

$$\frac{\mathrm{d}m_{\mathrm{a}}}{\mathrm{d}t} = -K\sigma m^{2/3}\rho_{\mathrm{air}}v^3, \tag{2}$$

where K is the shape density coefficient, m is the meteoroid mass (m_{a} is the ablated mass), t is the time, v is the velocity, ρ_{air} is the atmosphere bulk density (NRLMSISE-00 model[75]) and σ is the ablation coefficient. The ablation coefficient regulates how much mass is removed from the meteoroid per unit energy, and is usually expressed in kg MJ^{-1} (s^2 km^{-2} is also often found in the literature). The parameter K is used because the meteoroid density and shape cannot be measured separately:

$$K = \Gamma A\rho_{\mathrm{m}}^{-2/3}, \tag{3}$$

where Γ is the drag coefficient, A is the shape coefficient (1.21 for spheres, which we adopt) and ρ_{m} is the meteoroid (or grain) bulk density. The equations were numerically integrated using a fourth-order Runge–Kutta method and a time step of 2 ms. The integration of individual fragments is stopped if their mass falls below 10^{-14} kg or the speed below 3 km s^{-1}, which is the ablation limit[61].

The luminosity produced by ablation is computed as:

$$I = -\tau\frac{v^2}{2}\frac{\mathrm{d}m_{\mathrm{a}}}{\mathrm{d}t} + mv\frac{\mathrm{d}v}{\mathrm{d}t}, \tag{4}$$

where τ is the luminous efficiency. In this work, we use the modern luminous efficiency function of ref. [49] to model the observed event.

If the meteoroid or an ejected fragment is set to erode at a given time in the model, the total mass lost in erosion is regulated by the erosion coefficient η, which is applied in the same manner as the ablation coefficient in equation (2):

$$\frac{\mathrm{d}m_{\mathrm{e}}}{\mathrm{d}t} = -K\eta m^{2/3}\rho_{\mathrm{air}}v^3. \tag{5}$$

For grain bulk density, we use 3,500 kg m^{-3}, appropriate for refractory silicate grains. The total mass loss at a given time is then the sum of the ablation and erosion mass loss:

$$\frac{\mathrm{d}m}{\mathrm{d}t} = \frac{\mathrm{d}m_{\mathrm{a}}}{\mathrm{d}t} + \frac{\mathrm{d}m_{\mathrm{e}}}{\mathrm{d}t}. \tag{6}$$

Inspired by in situ observations of the mass distribution of cometary dust[53], the masses of eroded grains are distributed according to a power law $n(m) \approx m^{-s}$ (ref. [76]), where $n(m)$ is the number of grains of a given mass m, and s is the differential mass distribution index. An upper (m_{u}) and a lower (m_{l}) grain mass limit is set during the modelling. To speed up computation, this mass range is binned into z bins per order of magnitude; thus, the integration of ablation equations is done only once for every mass bin instead for every fragment. A mass sorting parameter can be defined as $p = 10^{1/z}$ and it follows that the total number of grain mass bins within a range of masses is $k = \lfloor \log(m_{\mathrm{l}}/m_{\mathrm{u}})/\log p \rfloor$ The total number of grains having a mass equal to the upper mass limit is then:

$$n_{\mathrm{u}} = \begin{cases} \frac{m_{\mathrm{e}}}{km_{\mathrm{u}}}, & \text{for } s = 2 \\ \frac{m_{\mathrm{e}}}{m_{\mathrm{u}}}\frac{1-p^{(2-s)}}{1-p^{k(2-s)}}, & \text{for } s \neq 2, \end{cases} \tag{7}$$

where m_{e} is the total eroded mass at the given time step. The mass of every bin i is then $m_i = m_{\mathrm{u}}p^i$ for $i = 0, 1, \ldots, k-1$. The number of discrete grains N_i in every bin can be computed as:

$$n_i = n_{\mathrm{u}}(m_{\mathrm{u}}/m_i)^{(s-1)} + \frac{\Delta m_{i-1}}{m_i}, \tag{8}$$

$$N_i = \lfloor n_i \rfloor, \tag{9}$$

where $\Delta m_i = m_i(n_i - N_i)$ is the leftover mass in the mass bin after making the number of grains discrete ($\Delta m_0 = 0$). The leftover mass from the larger-mass bins is distributed into smaller-mass bins to ensure that there is no 'virtual' mass loss due to numerical rounding. The grains are then ablated as single bodies until exhaustion following equations (1) and (2). A separate luminosity I_i is computed for every mass bin, and the total luminosity produced by all grains at a given time is simply $\sum_{i=0}^{k-1} N_i I_i$.

Finally, after all fragments and grains have been fully integrated and their masses depleted, the magnitude M of the fireball as it would have be seen at a distance of 100 km is computed as:

$$M = -2.5\log\frac{I}{P_{0\mathrm{m}}}, \tag{10}$$

where $P_{0\mathrm{m}}$ is the power that a meteor needs to radiate in the camera's spectral band pass so that it has an apparent magnitude of 0 mag at a range of 100 km. In this work, we use a value of 1,300 W, as appropriate for a high-speed meteor in the spectral band pass of silicon sensors[77].

Meteoroid strength and dynamic pressure

From decades of observations, it is now well established that there is a strong correlation between meteoroid material type and bulk strength[78]. Cometary meteoroids are weak and disrupt under dynamic pressures of ~1 kPa (ref. [61]) upon entering the atmosphere, whereas asteroidal meteoroids can withstand pressures of 100 kPa before any fragmentation[49], with their strongest components withstanding pressures of up to 1–10 MPa without catastrophic disruption[79]. These differing strengths explain why cometary fireballs break up at heights above 70 km (ref. [1]), whereas meteorite-dropping fireballs break up typically below 40 km (ref. [49]). For cometary meteoroids, the strength of constituent 10–300 µm silicate grains is on the order of tens of

megapascals[80], but high porosity reduces the strength of larger grain aggregates by several orders of magnitude[81].

Meteoroid fragmentation is commonly assumed to occur when the dynamic pressure $P_{dyn} = \Gamma\rho_{air}v^2$ exceeds the mechanical strength of the body[76]. In most cases, meteorite-dropping fireballs of asteroidal origin fragment in two phases: the first from 0.04 MPa to 0.12 MPa and the second from 0.5 MPa to 5 MPa (ref. [49]). These are markedly lower than the tensile strengths of ordinary chondrites that survive atmospheric flight and are recovered, which are measured to be between 20 MPa and 40 MPa (ref. [9]). Rarely, meteoroids act like monoliths and show no evidence of fragmentation[82], possibly due to a lack of internal cracking, which is commonly invoked as the mechanism that causes fragmentation at lower strengths[78]. As we model fragmentation directly and use both the light curve and the dynamics as a constraint, the derived values should be accurate to within ±25%, which is the short-term variation in the atmosphere mass density that is not captured by current atmosphere models[83].

Computing PE

The PE criterion was derived as an empirical tool to help easily differentiate between different material types[48] without the complexity of full numerical ablation modelling. It was based on well-understood relationships between physical properties of meteoroids and their observed behaviour as they enter the atmosphere.

It is defined as:

$$\mathrm{PE} = \log\rho_E - 0.42\log m_0 + 1.49\log v_0 - 1.29\log\cos Z_C \quad (11)$$

where ρ_E is the atmosphere mass density at the end height of the fireball in g cm^{-3}, m_0 is the initial mass in g, v_0 is the initial velocity in km s^{-1} and Z_C is the zenith angle.

Note that for the PE criterion to be properly computed, the correct mass scale (as outlined in refs. [8,48]) needs to be used. In general, initial meteoroid mass is computed by integrating the total observed light production, assuming a spectral distribution P_{0m} and a luminous efficiency τ (ref. [84]):

$$m = \frac{2P_{0m}}{\tau v^2}\int_0^t 10^{-0.4M(t)} \quad (12)$$

where $M(t)$ is the observed magnitude. As it enters the atmosphere, a meteoroid only possesses kinetic energy. The luminous efficiency measures how much of that kinetic energy gets converted into light and is usually on the order of a few percent.

PE was originally derived using the following luminous efficiency, which should always be used for PE computation:

$$\tau = \begin{cases} 1.5\times10^{-2.75}, & \text{for } v_0 \le 9.3\ \mathrm{km\,s^{-1}} \\ 1.5\times10^{-5.60+2.92\log v_0}, & \text{for } 9.3 < v_0 \le 12.5\ \mathrm{km\,s^{-1}} \\ 1.5\times10^{-3.24+0.77\log v_0}, & \text{for } 12.5 < v_0 \le 17.0\ \mathrm{km\,s^{-1}} \\ 1.5\times10^{-2.50+0.17\log v_0}, & \text{for } 17.0 < v_0 \le 27.0\ \mathrm{km\,s^{-1}} \\ 1.5\times10^{-3.69+1.00\log v_0}, & \text{otherwise} \end{cases} \quad (13)$$

where τ is the dimensionless luminous efficiency as a fraction (not percentage) and v_0 is the initial velocity in km s^{-1}.

These values of luminous efficiency are considered to be underestimated compared with contemporary models. For example, for the Alberta fireball with $v_0 = 62.1$ km s^{-1} the luminous efficiency according to equation (13) is $\tau = 1.9\%$, while in the modelling we used values between 10% and 14% (depending on the mass). To scale contemporary mass values to the appropriate values for PE computation, we simply scale the mass by the ratio of the historic (equation (13)) and modern[49] luminous efficiencies.

Strength of cometary material and cometary refractory inclusions

In situ measurement of the nucleus of comet 67P by the Philae lander found a surface compressive strength of 1–3 kPa (ref. [85]), a value consistent with in-atmosphere measurements of cometary meteoroid strength[83]. The probe stopped bouncing when it hit an area of crushing strength >4 MPa, possibly a processed, tightly packed 'sintered' surface layer[86] created by space weathering. Despite having a high crushing strength, the surface layer was also found to have a high porosity of 30% to 65%. The best fit to data was found by using a surface bulk density of 470 ± 45 kg m^{-3} (ref. [87]).

To explain Philae lander measurements, modelling of sintering for the comet 67P has shown that a hardened surface layer (compressive strength 8 MPa) several metres thick can be formed due to space weathering[88]. However, the model found that the tensile strength (what is traditionally measured during atmospheric entry of meteoroids[89]) of this layer is an order of magnitude lower.

The possibility of meteorite delivery from the outer Solar System was discussed in detail by ref. [90]. Using a numerical model that included radioactive decay of short-lived nuclides and exothermic crystallization of amorphous water ice to crystalline ice as sources of heat, they explored whether it was possible to sustain liquid water in comets for 1 kyr to 1 Myr shortly after the formation of the Solar System, long enough for the hydrothermal alteration to produce CI chondritic material. They concluded that the transformation was possible, but discuss no possibility of forming ordinary chondritic material. We are unaware of any proposed physical process in the literature that can transform soft cometary material into material of similar bulk density and strength to OCs.

On the basis of all of the foregoing considerations, macroscopic samples of cometary surface layers are expected to have smaller bulk densities than monolithic silicate material. Nevertheless, cometary material can have millimetre-sized inclusions of stronger material such as calcium–aluminium-rich inclusions, as found in the dust of comets Wild 2[91] and 67P[92]. In addition, some millimetre-sized components of Taurid meteoroids (from 2P/Encke) were found to withstand pressures of up to 300 kPa (refs. [60,93]), and strong millimetre-sized inclusions have been found in Leonid meteoroids (from an HTC 55P/Tempel–Tuttle)[57].

Most recently, a survey[10] of millimetre-sized meteoroids that analysed their spectral and fragmentation properties identified two iron meteoroids on HTC orbits (out of a total of 64 HTC meteors). The authors suggested that these were ejected during the formation of the Solar System due to the dynamical instability caused by Jupiter's migration.

Astrometric calibration

The most critical measurement leading to the core result in this work (the unusually low end height for such a high-velocity fireball) is directly derived from optical observations of the event. Thus, the quality of the astrometric calibration and measurements is of paramount importance. In this section, we present the calibration details for each of the three optical instruments used to derive the trajectory. These include two dedicated high-resolution GFO fireball cameras (one at Miquelon Lake and the other near Vermilion, Alberta) and one security camera (located in Cochrane, Alberta, outside of Calgary). The camera locations are given in Supplementary Table 1 and shown in relation to the fireball in Extended Data Fig. 1.

GFO data. The GFO all-sky cameras operated by the MORP2.0 project produce 7,340 × 4,930 pixel colour images with an exposure time of 27 s and 14 bits of depth. Electronic liquid crystal shutters are toggled to encode the timing information into the image. The shutters produce 20 segments per second, and the segments are encoded as a de Brujin sequence of ones and zeros[94] so that the absolute time of every segment can be derived to an accuracy of 1 ms. In combination with the Samyang 8 mm f/3.5 fish-eye lens, the images have a plate scale of 2 arcmin px^{-1}.

The data produced by these cameras are of similar quality and have a similar sensitivity limit to other fireball networks.

The astrometric fit was performed with a radial distortion model[5] using odd polynomial coefficients up to the seventh-order, asymmetry correction, and a fixed aspect ratio. Including the pointing direction (reference right ascension, declination, position angle and the plate scale), the fit uses a total of 11 free parameters.

Extended Data Fig. 2 shows the fit residuals for the Miquelon Lake camera. The mean angular forward mapping (image to sky) error was 0.49 arcmin, with a fit showing no trends in residuals with radius from the centre of the image but a slight systematic trend in the azimuth. We believe that the main cause of the trend is a higher-order component of asymmetry in the optics not captured by the distortion model, as the point-spread function varied across the field of view. Nevertheless, this offset is only on the order of 0.5 arcmin, that is 20 m at the range of the fireball from the station, and does not significantly influence the final result. The fireball covered azimuths from 30° to 350° (anticlockwise) and elevations from 54° to 15.7°, ranges well covered by available calibration stars.

The astrometric fit for the Vermilion GFO station was not as good, having root-mean-square-fit residuals of 1.37 arcmin, as shown in Extended Data Fig. 3. This decrease in accuracy was caused by a more non-Gaussian point-spread function than for the Miquelon Lake camera. However, the absolute accuracy remained high—the corresponding linear error was only 65 m at the range of the fireball. The fireball had a nearly constant azimuth of 310° and covered elevations from 43° to 11°, ranges for which there were many stars in the calibration.

Security camera calibration

Despite the good geometry and high accuracy of GFO measurements (convergence angle of 46. 5° and spatial trajectory fit residuals of ~30 m), a two-station trajectory solution can suffer from systematic biases due to meteor-station geometry[95,96]. As a further constraint, we included additional measurements from a Google Nest doorbell camera in Cochrane, Alberta, 50 km west of Calgary.

The radial distortion model with odd terms up to the fifth order was used for calibration[5]. The model has a total of eight parameters and eight stars were used in the fit (Extended Data Fig. 4). The average fit error was 4 arcmin. Only the first half of the fireball was used in the trajectory solution as the camera saturated and skipped frames during the brightest phase. The difference in the geocentric radiant with and without the security camera measurements was only 0.03°, and 0.14 km s^{-1} in geocentric speed, indicating that the GFO-only solution had no major systematic errors.

Photometric calibration

To fully model the fragmentation behaviour of a meteoroid, it is necessary to have a well-calibrated light curve. The Alberta event was observed by both space-based GLM instruments and one fixed GoPro HERO5 action camera in Calgary (~400 km from the fireball). Note that the GFO cameras used for astrometry were partially saturated over the height range of interest and therefore not used in the photometric calibration. However, as the Nikon D810 used by the GFO has complementary metal–oxide–semiconductor (CMOS) chips for imaging, and not charge-coupled device (CCD) sensors, the astrometric position picks are reliable even in saturation[5].

The GoPro camera had a low sensitivity and, in conjunction with the large range to the fireball, it was able to capture the whole fireball without saturating despite only having 8 bits of depth. As the camera did not observe any stars, the absolute calibration was done indirectly using seven distant streetlights visible in the video (a similar method was previously successfully applied in refs. [97,98]). A separate digital single-lens reflex (DSLR) photograph of stars and the streetlights was taken by placing the DSLR camera next to the GoPro camera—the apparent magnitudes of the streetlights were measured on the DSLR photo and used as a basis for the GoPro calibration. The mean photometric error was ±0.27 mag and the vignetting coefficient was estimated to be 0.001 rad px^{-1} (see ref. [5]).

An attempt was made to measure the photometry from scattered light on the Cochrane security camera video (method of ref. [97]), but the camera had a wide-dynamic-range feature. This produces image levels that are not linear responses to light and was thus not able to be used. Such image enhancement features may prevent using modern security cameras for scattered light fireball photometry in the future.

Converting the energy observed by the GLM into magnitudes is challenging due to its narrow 1.1 nm pass band around 777. nm, making it necessary to assume a spectral energy distribution to compute a bolometric magnitude. For slower meteoroids such as meteorite-dropping fireballs, it is possible to assume a black-body spectrum and derive a conversion[7], but at high speeds, elemental and atmospheric lines are more pronounced making the black-body assumption invalid. Furthermore, the intensity of the oxygen triplet line that the GLM is observing was found to significantly increase with meteoroid speed[99]. For these reasons, we performed a manual calibration between the GLM group energy and magnitude using three fast and bright (around −11 mag) fireballs observed by the NASA Meteoroid Environment Office[100] and All-sky Meteor Orbit System (AMOS) all-sky cameras[2]. Among many fireballs observed by these systems, only two fireballs observed with NASA systems had GLM light curves and were observed sufficiently far away not to saturate the cameras. Some saturated frames in the AMOS recording (19 October 2020, 12:42:55 UTC) were corrected using a calibration curve for saturated pixels, based on calibrated measurements of bright planets and the Moon in different phases. The in-atmosphere speeds of the fireballs were 58 km s^{-1}, 66 km s^{-1} and 69 km s^{-1}, comparable to the Alberta fireball. We used the classical equation to compute the magnitude:

$$M = -2.5 \log E_G + p_0 \quad (14)$$

where E_G is the GLM group energy in femtojoules and the p_0 is the photometric offset in magnitudes. For all three fireballs, the GLM light curves matched best for $p_0 = -9.2$, with an error of ±0.1 mag. The comparison between the optical and GLM light curves is shown in Extended Data Fig. 5.

Trajectory details

Supplementary Table 2 details the parameters of the start and end points of the fireball. Extended Data Fig. 6 shows the trajectory fit residuals and the observed deceleration. The trajectory fit is tight and within the expected astrometric accuracy. The fireball did not show much deceleration before a height of 60 km. The initial velocity was computed as the average velocity above the height of 70 km.

The reference time for the trajectory is 22 February 2021, 13:23:17.683 UTC (Julian date 2,459,268.057843548711). The state vector in the Earth-centred inertial coordinates in the epoch of date is given in Supplementary Table 3, the state vector covariance matrix is given in Supplementary Table 4 and the orbital covariance matrix is given in Supplementary Table 5.

Orbital integration

To investigate the influence of planetary interactions with the meteoroid's orbit, we backtracked 100 clones within the measured uncertainty. The RADAU[101] 15th-order integrator was used with an error tolerance of 10^{-12} and an external time step of 1 day. Because of its high inclination, the only appreciable approaches to the planets are at its other (ascending) node, which is near Mars' orbit. However, no clone passed closer than 1.1 au from this planet. Extended Data Fig. 7 shows the variation in the heliocentric elements as a function of distance from Mars. The simulations start 60 days before impact and run for 365 days further back. A slight jump in each of the elements can be seen at the minimum

distance from Mars, but it is small: it will not affect a potential parent body search and does not affect the proposed origin of the object.

Note that the orbital elements do not become completely constant even well after the Mars encounter. This is because they are heliocentric elements, and for such a large semi-major axis orbit, Jupiter's tug on both the Sun and the object creates ongoing small changes. Even if the orbital elements were considered in the barycentric frame, the effect of ongoing planetary perturbations on such loosely bound orbits means that the orbital elements will have trends over time regardless of the reference frame.

An extended integration backwards over 2,000 years, corresponding to several orbits of the clones, reveals that planetary perturbations have had only a small effect on the orbital elements of the meteoroid over this time span (Extended Data Fig. 8).

Ablation modelling results

We model the fragmentation behaviour of the fireball in two ways: (1) by direct erosion of the main body, and (2) by ejecting larger fragments that erode independently. Extended Data Fig. 9 shows the details of the fragmentation on the simulated light curve, which are also listed in Supplementary Table 6, and Extended Data Fig. 10 shows the mass loss with increasing dynamic pressure. The modelled physical properties of the fireball are given in Supplementary Table 7. We provide only a single solution with no error estimate. The model is fit manually and a still unresolved question in the field is how to provide meaningful model uncertainties. The model is highly nonlinear and defining a robust cost function has also not yet been addressed. Previous attempts to automate the model fits ignored either the dynamics or the photometric measurements, and failed to model the fragmentation directly[102–104]. In our approach, we use the dynamics as a hard constraint to accurately classify the material type, and include additional fragmentation details to explain light curve. This established method is often used to accurately model meteorite-dropping fireballs and accurately predict the masses of meteorites on the ground[54,72].

Because this fireball is one of the first of its type to be modelled (large, high-speed rocky meteoroid reaching low altitudes), there were several differences and uncertainties in chosen parameters compared with low-velocity type I objects:

(1) The luminous efficiency for type I objects at high speeds is unknown, as this is one of the first objects of this kind to be observed. We used the model of ref. [49], which suggests a value of ~14% for 1 kg objects and ~10% for grains. If the luminous efficiency is akin to a low-speed meteorite-dropping fireballs (~5%), the initial mass is ~3× larger (6 kg), but the identification of the meteoroid as a type I fireball is unchanged.
(2) A higher intrinsic ablation coefficient of 0.009 kg MJ^{-1} (and 0.007 kg MJ^{-1} below 60 km) was used, compared with 0.005 kg MJ^{-1} for low-velocity, deeply penetrating fireballs[61].
(3) The model matches the light curve well even at the beginning of luminous flight at fainter magnitudes. This is not usually the case for slower meteorite-dropping fireballs as they undergo a period of preheating[105], and the classical equations do not capture that complexity in those cases.

Data availability

The trajectory data are included with this article as Supplementary Data files. The raw images and Supplementary Information are available on Zenodo at https://doi.org/10.5281/zenodo.7225827. Source data are provided with this paper.

Code availability

The optical data were calibrated using the open source SkyFit2 software available in the RMS library at https://github.com/CroatianMeteorNetwork/RMS. The WesternMeteorPyLib (wmpl) library was used to compute the trajectory and fit the meteoroid ablation model to the observations. It is available at https://github.com/wmpg/WesternMeteorPyLib/.

References

1. Spurný, P., Borovička, J., Mucke, H. & Svoreň, J. Discovery of a new branch of the Taurid meteoroid stream as a real source of potentially hazardous bodies. *Astron. Astrophys.* **605**, A68 (2017).
2. Tóth, J. et al. AMOS—the Slovak worldwide all-sky meteor detection system. In *Proc. 1st NEO and Debris Detection Conference* Vol. 1 (eds Flohrer, T., Jehn, R. & Schmitz, F.) (ESA Space Safety Programme Office, 2019).
3. Devillepoix, H. et al. A global fireball observatory. *Planet. Space Sci.* **191**, 105036 (2020).
4. Colas, F. et al. FRIPON: a worldwide network to track incoming meteoroids. *Astron. Astrophys.* **644**, A53 (2020).
5. Vida, D. et al. The global meteor network—methodology and first results. *Mon. Not. R. Astron. Soc.* **506**, 5046–5074 (2021).
6. Goodman, S. J. et al. The GOES-R Geostationary Lightning Mapper (GLM). *Atmos. Res.* **125–126**, 34–49 (2013).
7. Jenniskens, P. et al. Detection of meteoroid impacts by the Geostationary Lightning Mapper on the GOES-16 satellite. *Meteorit. Planet. Sci.* **53**, 2445–2469 (2018).
8. Ceplecha, Z. Earth's influx of different populations of sporadic meteoroids from photographic and television data. *Bull. Astron. Inst. Czechoslov.* **39**, 221–236 (1988).
9. Flynn, G. J., Consolmagno, G. J., Brown, P. & Macke, R. J. Physical properties of the stone meteorites: implications for the properties of their parent bodies. *Geochemistry* **78**, 269–298 (2018).
10. Vojáček, V., Borovička, J., Koten, P., Spurný, P. & Štork, R. Properties of small meteoroids studied by meteor video observations. *Astron. Astrophys.* **621**, A68 (2019).
11. Binzel, R. P., Reddy, V. & Dunn, T. The near-Earth object population: connections to comets, main-belt asteroids, and meteorites. *Asteroids IV* **1**, 243 (2015).
12. Weissman, P. R., A'Hearn, M. F., McFadden, L. & Rickman, H. Evolution of comets into asteroids. *Asteroids III* **1**, 669 (2002).
13. Brownlee, D., Joswiak, D. & Matrajt, G. Overview of the rocky component of Wild 2 comet samples: insight into the early solar system, relationship with meteoritic materials and the differences between comets and asteroids. *Meteorit. Planet. Sci.* **47**, 453–470 (2012).
14. Weissman, P. R. & Levison, H. F. Origin and evolution of the unusual object 1996 PW: asteroids from the Oort cloud? *Astrophys. J. Lett.* **488**, L133 (1997).
15. Shannon, A., Jackson, A. P., Veras, D. & Wyatt, M. Eight billion asteroids in the Oort cloud. *Mon. Not. R. Astron. Soc.* **446**, 2059–2064 (2015).
16. Meech, K. J. et al. Inner Solar System material discovered in the Oort cloud. *Sci. Adv.* **2**, e1600038 (2016).
17. Shannon, A., Jackson, A. P. & Wyatt, M. C. Oort cloud asteroids: collisional evolution, the nice model, and the Grand Tack. *Mon. Not. R. Astron. Soc.* **485**, 5511–5518 (2019).
18. Walsh, K. J., Morbidelli, A., Raymond, S. N., O'Brien, D. P. & Mandell, A. M. A low mass for Mars from Jupiter's early gas-driven migration. *Nature* **475**, 206–209 (2011).
19. Meech, K. et al. Origin of Earth's water: sources and constraints. *Planet. Astrobiol.* **325** (2020).
20. Izidoro, A., de Souza Torres, K., Winter, O. & Haghighipour, N. A compound model for the origin of earth's water. *Astrophys. J.* **767**, 54 (2013).
21. Raymond, S. N., Boulet, T., Izidoro, A., Esteves, L. & Bitsch, B. Migration-driven diversity of super-Earth compositions. *Mon. Not. R. Astron. Soc. Lett.* **479**, L81–L85 (2018).

22. Zwart, S. P. Oort cloud ecology—I. Extra-solar Oort clouds and the origin of asteroidal interlopers. *Astron. Astrophys.* **647**, A136 (2021).
23. Bottke Jr, W. F. et al. The fossilized size distribution of the main asteroid belt. *Icarus* **175**, 111–140 (2005).
24. Minton, D. A. & Malhotra, R. Dynamical erosion of the asteroid belt and implications for large impacts in the inner Solar System. *Icarus* **207**, 744–757 (2010).
25. Clement, M. S., Raymond, S. N. & Kaib, N. A. Excitation and depletion of the asteroid belt in the early instability scenario. *Astron. J.* **157**, 38 (2019).
26. de Sousa Ribeiro, R. et al. Dynamical evidence for an early giant planet instability. *Icarus* **339**, 113605 (2020).
27. Marrocchi, Y., Delbo, M. & Gounelle, M. The astrophysical context of collision processes in meteorites. *Meteorit. Planet. Sci.* **56**, 1406–1421 (2021).
28. Bitsch, B., Lambrechts, M. & Johansen, A. The growth of planets by pebble accretion in evolving protoplanetary discs. *Astron. Astrophys.* **582**, A112 (2015).
29. Morbidelli, A. & Raymond, S. N. Challenges in planet formation. *J. Geophys. Res. Planets* **121**, 1962–1980 (2016).
30. Johansen, A. et al. Rapid planetesimal formation in turbulent circumstellar disks. *Nature* **448**, 1022–1025 (2007).
31. Levison, H. F., Kretke, K. A. & Duncan, M. J. Growing the gas-giant planets by the gradual accumulation of pebbles. *Nature* **524**, 322–324 (2015).
32. Raymond, S. N. & Izidoro, A. The empty primordial asteroid belt. *Sci. Adv.* **3**, e1701138 (2017).
33. Raymond, S. N. & Izidoro, A. Origin of water in the inner Solar System: planetesimals scattered inward during Jupiter and Saturn's rapid gas accretion. *Icarus* **297**, 134–148 (2017).
34. Clement, M. S., Kaib, N. A., Raymond, S. N., Chambers, J. E. & Walsh, K. J. The early instability scenario: terrestrial planet formation during the giant planet instability, and the effect of collisional fragmentation. *Icarus* **321**, 778–790 (2019).
35. Brož, M., Chrenko, O., Nesvorný, D. & Dauphas, N. Early terrestrial planet formation by torque-driven convergent migration of planetary embryos. *Nat. Astron.* **5**, 898–902 (2021).
36. DeSouza, S. R., Roig, F. & Nesvorný, D. Can a jumping-Jupiter trigger the moon's formation impact? *Mon. Not. R. Astron. Soc.* **507**, 539–547 (2021).
37. Bitsch, B., Morbidelli, A., Lega, E. & Crida, A. Stellar irradiated discs and implications on migration of embedded planets—II. Accreting-discs. *Astron. Astrophys.* **564**, A135 (2014).
38. Hicks, M., Buratti, B., Newburn Jr, R. & Rabinowitz, D. Physical observations of 1996 PW and 1997 SE5: extinct comets or D-type asteroids? *Icarus* **143**, 354–359 (2000).
39. Lamy, P. & Toth, I. The colors of cometary nuclei—comparison with other primitive bodies of the Solar System and implications for their origin. *Icarus* **201**, 674–713 (2009).
40. DeMeo, F., Alexander, C., Walsh, K., Chapman, C. & Binzel, R. The compositional structure of the asteroid belt. *Asteroids IV* **1**, 13 (2015).
41. Meech, K. J. et al. C/2013 P2 Pan STARRS—the Manx comet. In *AAS/Division for Planetary Sciences Meeting 46* 200-02 (Smithsonian Astrophysical Observatory, 2014).
42. Stephens, H. et al. Chasing Manxes: long-period comets without tails. In *AAS/Division for Planetary Sciences Meeting 49* 420-02 (Smithsonian Astrophysical Observatory, 2017).
43. Piro, C. et al. Characterizing the Manx candidate A/2018 V3. *Planet. Sci. J.* **2**, 33 (2021).
44. Boe, B. et al. The orbit and size-frequency distribution of long period comets observed by Pan-STARRS1. *Icarus* **333**, 252–272 (2019).
45. Davidsson, B. et al. The primordial nucleus of comet 67P/Churyumov–Gerasimenko. *Astron. Astrophys.* **592**, A63 (2016).
46. Binzel, R. P. et al. Observed spectral properties of near-earth objects: results for population distribution, source regions, and space weathering processes. *Icarus* **170**, 259–294 (2004).
47. Kaluna, H. M., Masiero, J. R. & Meech, K. J. Space weathering trends among carbonaceous asteroids. *Icarus* **264**, 62–71 (2016).
48. Ceplecha, Z. & McCrosky, R. Fireball end heights: a diagnostic for the structure of meteoric material. *J. Geophys. Res.* **81**, 6257–6275 (1976).
49. Borovička, J., Spurný, P. & Shrbený, L. Two strengths of ordinary chondritic meteoroids as derived from their atmospheric fragmentation modeling. *Astron. J.* **160**, 42 (2020).
50. Brown, P., Spalding, R., ReVelle, D. O., Tagliaferri, E. & Worden, S. The flux of small near-Earth objects colliding with the Earth. *Nature* **420**, 294–296 (2002).
51. Borovička, J., Spurný, P. & Koten, P. Atmospheric deceleration and light curves of draconid meteors and implications for the structure of cometary dust. *Astron. Astrophys.* **473**, 661–672 (2007).
52. Hulfeld, L., Küchlin, S. & Jenny, P. Three dimensional atmospheric entry simulation of a high altitude cometary dustball meteoroid. *Astron. Astrophys.* **650**, A101 (2021).
53. Hornung, K. et al. A first assessment of the strength of cometary particles collected in-situ by the COSIMA instrument onboard ROSETTA. *Planet. Space Sci.* **133**, 63–75 (2016).
54. Borovička, J. et al. The Košice meteorite fall: atmospheric trajectory, fragmentation, and orbit. *Meteorit. Planet. Sci.* **48**, 1757–1779 (2013).
55. Spurný, P. & Borovicka, J. in *Meteroids 1998* (eds Baggaley, W. J. & Porubcan, V.) 143–148 (Astronomical Institute of the Slovak Academy of Sciences, 1999).
56. Spurný, P. & Borovicka, J. Detection of a high density meteoroid on cometary orbit. In *IAU Colloquium 173: Evolution and Source Regions of Asteroids and Comets* (eds Svoren, J., Pittich, E. M. & Rickman, H.) 163–168 (Astronomical Institute of the Slovak Academy of Sciences, 1999).
57. Borovička, J. & Jenniskens, P. Time resolved spectroscopy of a Leonid fireball afterglow. *Earth Moon Planets* **82**, 399–428 (2000).
58. Kokhirova, G. & Borovička, J. Observations of the 2009 Leonid activity by the Tajikistan Fireball Network. *Astron. Astrophys.* **533**, A115 (2011).
59. Borovička, J. et al. *Physical and Chemical Properties of Meteoroids* (eds Ryabova, G. O., Asher, D. J. & Campbell-Brown, M. D.) 37–62 (Cambridge Univ. Press, 2019).
60. Borovička, J. & Spurny`, P. Physical properties of taurid meteoroids of various sizes. *Planet. Space Sci.* **182**, 104849 (2020).
61. Ceplecha, Z. et al. Meteor phenomena and bodies. *Space Sci. Rev.* **84**, 327–471 (1998).
62. Revelle, D. O. & Ceplecha, Z. Bolide physical theory with application to PN and EN fireballs. In *Meteoroids 2001 Conference*, *ESA Special Publication* Vol. 495 (ed. Warmbein, B.) 507–512 (ESA Publications Division, 2001).
63. Halliday, I., Griffin, A. A. & Blackwell, A. T. Detailed data for 259 fireballs from the Canadian Camera Network and inferences concerning the influx of large meteoroids. *Meteorit. Planet. Sci.* **31**, 185–217 (1996).
64. Vida, D., Campbell-Brown, M., Brown, P. G., Egal, A. & Mazur, M. J. A new method for measuring the meteor mass index: application to the 2018 Draconid meteor shower outburst. *Astron. Astrophys.* **635**, A153 (2020).
65. Ulm, K. Simple method to calculate the confidence interval of a standardized mortality ratio (SMR). *Am. J. Epidemiol.* **131**, 373–375 (1990).
66. Oberst, J. et al. The 'European Fireball Network': current status and future prospects. *Meteorit. Planet. Sci.* **33**, 49–56 (1998).

67. Levison, H. F., Duncan, M. J., Brasser, R. & Kaufmann, D. E. Capture of the Sun's Oort cloud from stars in its birth cluster. *Science* **329**, 187–190 (2010).
68. Stern, S. A. Collisions in the Oort cloud. *Icarus* **73**, 499–507 (1988).
69. Stern, S. A. The evolution of comets in the Oort cloud and Kuiper belt. *Nature* **424**, 639–642 (2003).
70. Weissman, P. R. in *Completing the Inventory of the Solar System* Vol. 107 (eds Rettig, T. W. & Hahn, J. M.) 265–288 (Astronomical Society of the Pacific, 1996).
71. Stern, S. A. ISM-induced erosion and gas-dynamical drag in the Oort cloud. *Icarus* **84**, 447–466 (1990).
72. Borovička, J. et al. The instrumentally recorded fall of the Križevci meteorite, Croatia, February 4, 2011. *Meteorit. Planet. Sci.* **50**, 1244–1259 (2015).
73. Borovička, J., Spurný, P., Grigore, V. I. & Svoreň, J. The January 7, 2015, superbolide over Romania and structural diversity of meter-sized asteroids. *Planet. Space Sci.* **143**, 147–158 (2017).
74. Borovička, J., Popova, O. & Spurný, P. The Maribo CM 2 meteorite fall—survival of weak material at high entry speed. *Meteorit. Planet. Sci.* **54**, 1024–1041 (2019).
75. Picone, J., Hedin, A., Drob, D. P. & Aikin, A. NRLMSISE-00 empirical model of the atmosphere: statistical comparisons and scientific issues. *J. Geophys. Res. Space Phys.* **107**, 1468 (2002).
76. Popova, O., Borovicka, J. & Campbell-Brown, M. in *Meteoroids: Sources of Meteors on Earth and Beyond* Vol. 25, 9–36 (eds Ryabova, G. O., Asher, D. J. & Campbell-Brown, M. D.) (Cambridge Univ. Press, 2019).
77. Weryk, R. J. & Brown, P. G. Simultaneous radar and video meteors—II: Photometry and ionisation. *Planet. Space Sci.* **81**, 32–47 (2013).
78. Borovička, J. Physical and chemical properties of meteoroids as deduced from observations. *Proce. IAU* **1**, 249–271 (2005).
79. Borovička, J., Popova, O., Nemtchinov, I., Spurný, P. & Ceplecha, Z. Bolides produced by impacts of large meteoroids into the Earth's atmosphere: comparison of theory with observations. I. Benesov bolide dynamics and fragmentation. *Astrono. Astrophys.* **334**, 713–728 (1998).
80. Brownlee, D. et al. Comet 81P/Wild 2 under a microscope. *Science* **314**, 1711–1716 (2006).
81. Kimura, H. et al. The tensile strength of dust aggregates consisting of small elastic grains: constraints on the size of condensates in protoplanetary discs. *Mon. Not. R. Astron. Soc.* **496**, 1667–1682 (2020).
82. Borovička, J. & Spurný, P. The Carancas meteorite impact—encounter with a monolithic meteoroid. *Astron. Astrophys.* **485**, L1–L4 (2008).
83. Vida, D. et al. High precision meteor observations with the Canadian Automated Meteor Observatory: data reduction pipeline and application to meteoroid mechanical strength measurements. *Icarus* **354**, 114097 (2021).
84. Vida, D., Brown, P. G. & Campbell-Brown, M. Modelling the measurement accuracy of pre-atmosphere velocities of meteoroids. *Mon. Not. R. Astron. Soc.* **479**, 4307–4319 (2018).
85. Biele, J. et al. The landing(s) of Philae and inferences about comet surface mechanical properties. *Science* **349**, aaa9816 (2015).
86. Thomas, H., Ratke, L. & Kochan, H. Crushing strength of porous ice-mineral bodies—relevance for comets. *Adv. Space Res.* **14**, 207–216 (1994).
87. Spohn, T. et al. Thermal and mechanical properties of the near-surface layers of comet 67P/Churyumov–Gerasimenko. *Science* **349**, aab0464 (2015).
88. Kossacki, K. J., Spohn, T., Hagermann, A., Kaufmann, E. & Kührt, E. Comet 67P/Churyumov–Ggerasimenko: hardening of the sub-surface layer. *Icarus* **260**, 464–474 (2015).
89. Spurný, P. et al. The Bunburra rockhole meteorite fall in SW Australia: fireball trajectory, luminosity, dynamics, orbit, and impact position from photographic and photoelectric records. *Meteorit. Planet. Sci.* **47**, 163–185 (2012).
90. Gounelle, M. et al. Meteorites from the outer solar system. in *The Solar System Beyond Neptune* Vol. 592, 525–541 (eds Barucci, M. A., Boehnhardt, H., Cruikshank, D. P. & Morbidelli, A.) (University of Arizona Press, 2008).
91. Joswiak, D., Brownlee, D., Nguyen, A. & Messenger, S. Refractory materials in comet samples. *Meteorit. Planet. Sci.* **52**, 1612–1648 (2017).
92. Paquette, J. A. et al. Searching for calcium–aluminum-rich inclusions in cometary particles with ROSETTA/COSIMA. *Meteorit. Planet. Sci.* **51**, 1340–1352 (2016).
93. Matlovič, P., Tóth, J., Rudawska, R. & Kornoš, L. Spectra and physical properties of Taurid meteoroids. *Planet. Space Sci.* **143**, 104–115 (2017).
94. Howie, R. M. et al. Submillisecond fireball timing using de Bruijn timecodes. *Meteorit. Planet. Sci.* **52**, 1669–1682 (2017).
95. Vida, D., Gural, P. S., Brown, P. G., Campbell-Brown, M. & Wiegert, P. Estimating trajectories of meteors: an observational Monte Carlo approach—I. Theory. *Mon. Not. R. Astron. Soc.* **491**, 2688–2705 (2020).
96. Vida, D., Brown, P. G., Campbell-Brown, M., Wiegert, P. & Gural, P. S. Estimating trajectories of meteors: an observational Monte Carlo approach—II. Results. *Mon. Not. R. Astron. Soc.* **491**, 3996–4011 (2020).
97. Spurný, P. et al. Analysis of instrumental observations of the Jesenice meteorite fall on April 9, 2009. *Meteorit. Planet. Sci.* **45**, 1392–1407 (2010).
98. Brown, P. et al. The Hamburg meteorite fall: fireball trajectory, orbit, and dynamics. *Meteorit. Planet. Sci.* **54**, 2027–2045 (2019).
99. Šegon, D., Vukić, M., Šegon, M., Andreić, V. & Gural, P. S. Meteors in the near-infrared as seen in the Ondrejov catalogue of representative meteor spectra. In *Proc. International Meteor Conference* (eds Rudawska, R. et al.) 107–108 (International Meteor Organization, 2018).
100. Cooke, W. J. & Moser, D. E. The status of the NASA all sky fireball network. In *Proc. International Meteor Conference* (eds Gyssens, M. & Roggemans, P.) 9–12 (IMO, 2011).
101. Everhart, E. in *Dynamics of Comets: Their Origin and Evolution* (eds Carusi, A. & Valsecchi, G. B.) 185–202 (Kluwer, 1985).
102. Sansom, E. K., Bland, P., Paxman, J. & Towner, M. A novel approach to fireball modeling: the observable and the calculated. *Meteorit. Planet. Sci.* **50**, 1423–1435 (2015).
103. Sansom, E. K. et al. 3D meteoroid trajectories. *Icarus* **321**, 388–406 (2019).
104. Tárano, A. M., Wheeler, L. F., Close, S. & Mathias, D. L. Inference of meteoroid characteristics using a genetic algorithm. *Icarus* **329**, 270–281 (2019).
105. Spurný, P., Borovička, J. & Shrbený, L. The Žďár nad Sázavou meteorite fall: fireball trajectory, photometry, dynamics, fragmentation, orbit, and meteorite recovery. *Meteorit. Planet. Sci.* **55**, 376–401 (2020).
106. Subasinghe, D., Campbell-Brown, M. & Stokan, E. Luminous efficiency estimates of meteors—I. Uncertainty analysis. *Planet. Space Sci.* **143**, 71–77 (2017).

Acknowledgements

We thank R. Howell for first bringing this fireball to our attention and A. DesLauriers for providing raw footage from his security camera in Cochrane, AB. Funding for this work was provided in part through NASA co-operative agreement 80NSSC21M0073 (D.V., P.G.B.), by

the Natural Sciences and Engineering Research Council of Canada Discovery Grants programme (grant numbers RGPIN-2016-04433 and RGPIN-2018-05659; D.V., P.G.B.), the Canada Research Chairs programme (P.G.B.), the Slovak Research and Development Agency grant APVV-16-0148 and the Slovak Grant Agency for Science grant VEGA 1/0218/22 (P.M., J.T.).

Author contributions

D.V. coordinated the effort, performed the analysis, implemented the software and wrote the manuscript. P.G.B. initially coordinated the effort and provided scientific insight. H.A.R.D. computed an initial trajectory and provided the raw GFO data. P.W. made valuable scientific interpretations of the results and added a connection to recent comet discoveries, and performed the orbital integrations. D.E.M. helped digitize the MORP data, systematically collected and organized all casual recordings of the fireball, provided the GLM observations, and identified fireballs for GLM calibration. P.M. and J.T. provided observations of a fireball jointly observed with the AMOS system and the GLM. C.D.K.H. and P.J.A.H. provided the GFO data from the Miquelon Lake and Vermilion cameras and helped contact the local people who observed the fireball. E.K.S. and M.C.T. analysed the global GFO dataset to locate other fireballs of interest and provided data access. W.J.C. provided initial coordination. D.W.H. provided the GoPro video and took DSLR images for its photometric calibration.

Competing interests

The authors declare no competing interests.

Additional information

Extended data is available for this paper at https://doi.org/10.1038/s41550-022-01844-3.

Supplementary information The online version contains supplementary material available at https://doi.org/10.1038/s41550-022-01844-3.

Correspondence and requests for materials should be addressed to Denis Vida.

Peer review information *Nature Astronomy* thanks Petr Pokorny, Karen Meech and Peter Jenniskens for their contribution to the peer review of this work.

Reprints and permissions information is available at www.nature.com/reprints.

Publisher's note Springer Nature remains neutral with regard to jurisdictional claims in published maps and institutional affiliations.

https://doi.org/10.1038/s41550-022-01844-3

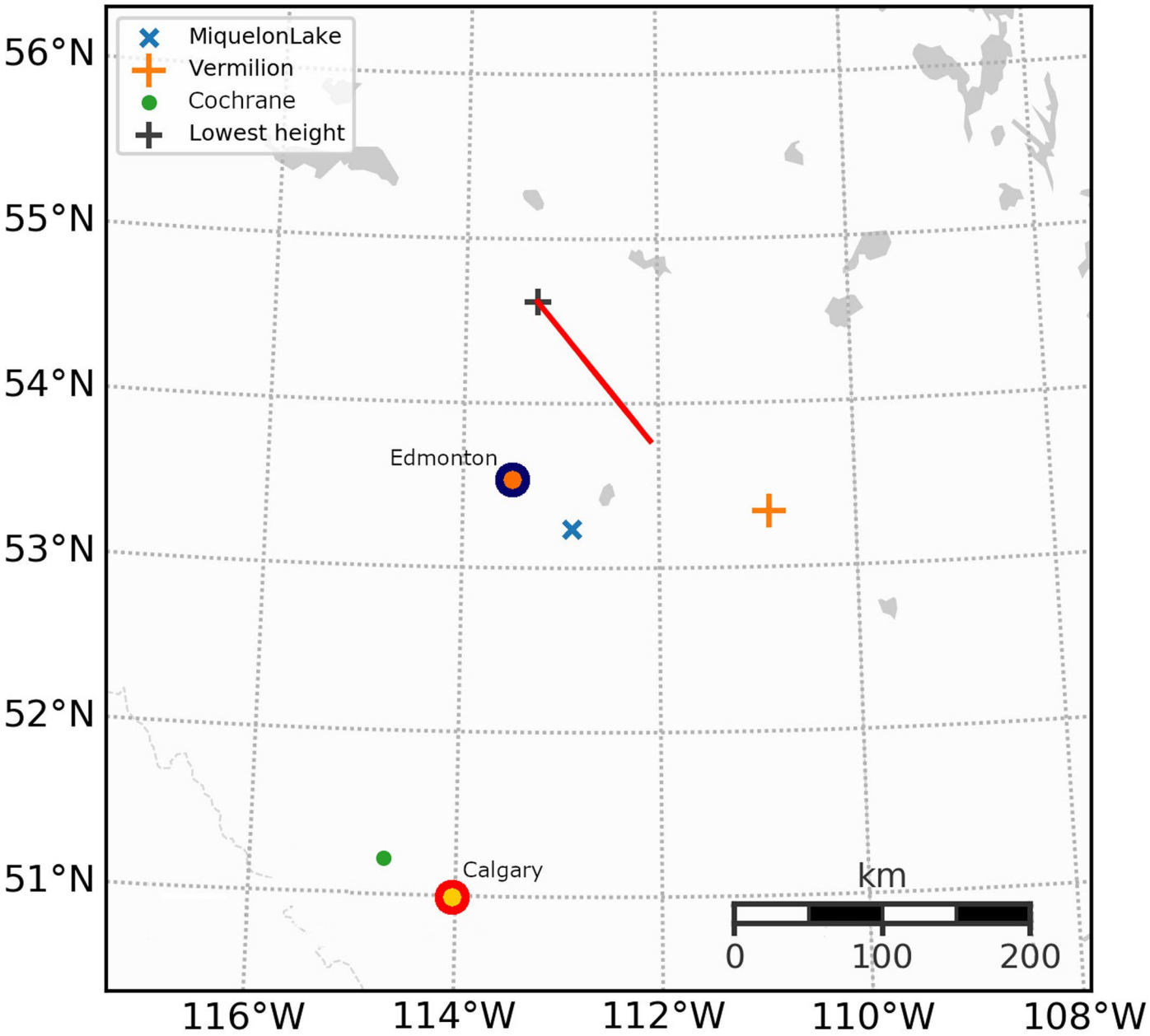

Extended Data Fig. 1 | Map showing the fireball track and the camera locations. Map showing the location of the fireball trajectory (red line), cameras, and major population centres in Calgary and Edmonton. The GoPro camera was located in Calgary.

https://doi.org/10.1038/s41550-022-01844-3

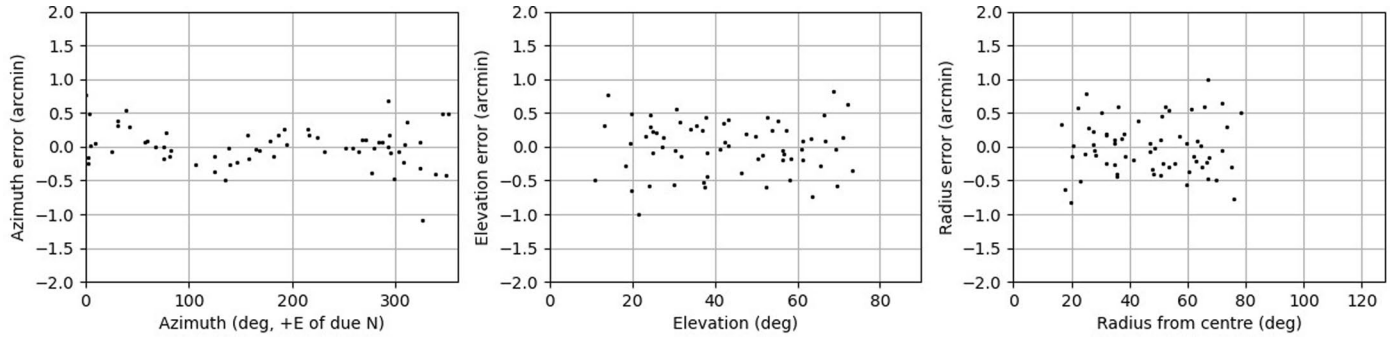

Extended Data Fig. 2 | Miquelon Lake camera astrometric calibration. Astrometric calibration fit using a 7th order polynomial (odd terms only) radial distortion model for the Miquelon Lake camera. Forward mapping (image to sky) errors.

https://doi.org/10.1038/s41550-022-01844-3

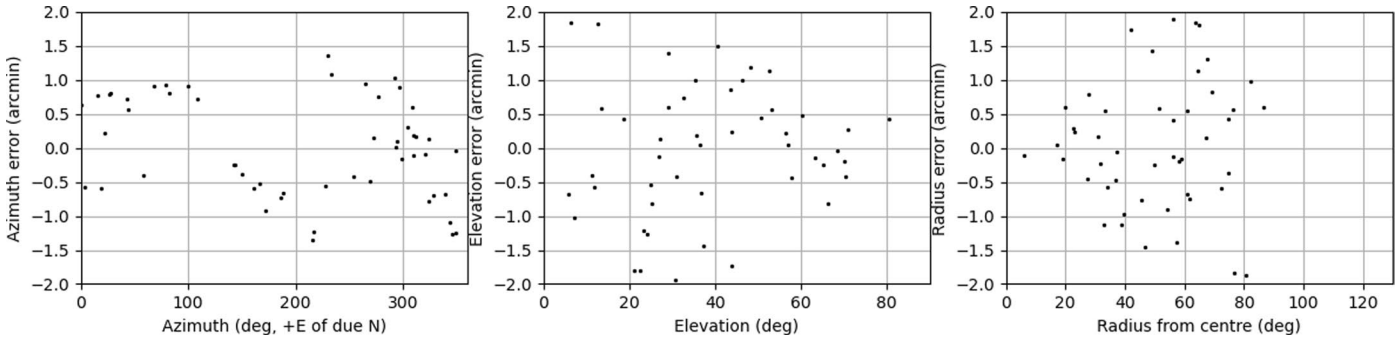

Extended Data Fig. 3 | Vermillion camera astrometric calibration. Astrometric calibration fit for the Vermillion camera. Forward mapping (image to sky) errors.

https://doi.org/10.1038/s41550-022-01844-3

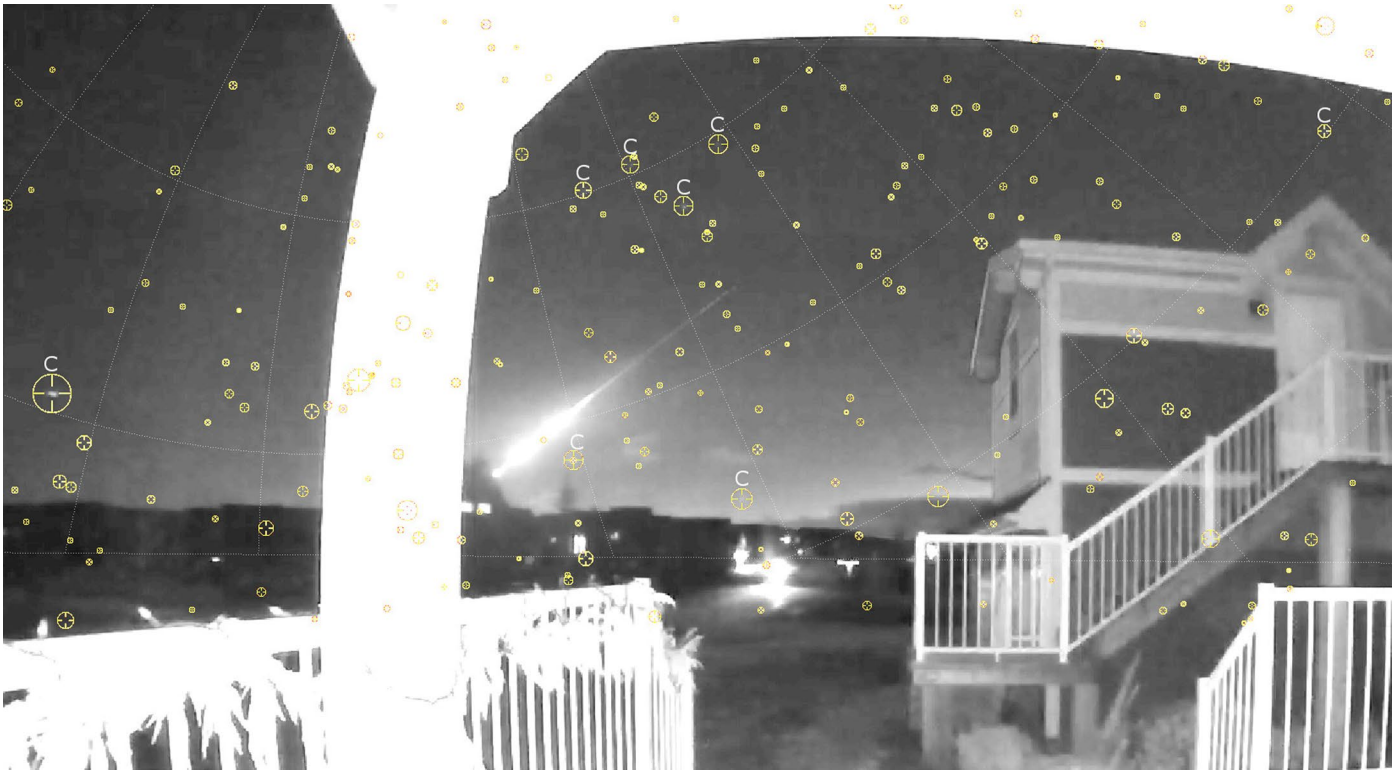

Extended Data Fig. 4 | Cochrane security camera astrometric calibration. Composite of frames from the Cochrane security camera video showing the fireball and the calibration stars (marked with a white letter C), four of which were in Cassiopeia. An equatorial grid is laid over the video with catalogue stars shown as yellow crosshairs. Credit: Airell DesLauriers.

https://doi.org/10.1038/s41550-022-01844-3

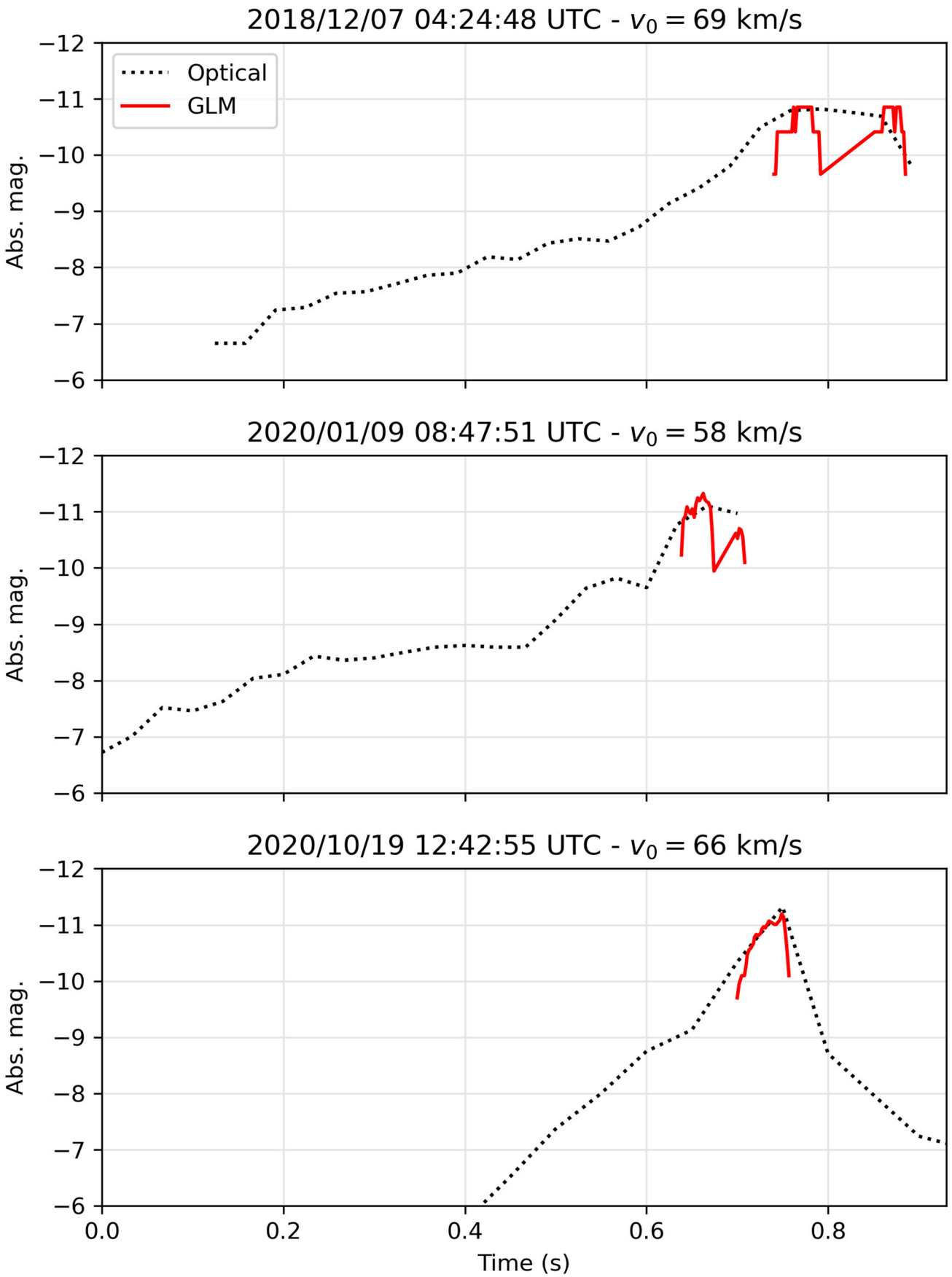

Extended Data Fig. 5 | Comparison between optical light curves and GLM-derived light curves of calibration fireballs. The optical light curves (dotted curves) were derived from ground-based sensors, and the GLM light curves (red curves) were derived from the GOES-16 and 17 satellites.

https://doi.org/10.1038/s41550-022-01844-3

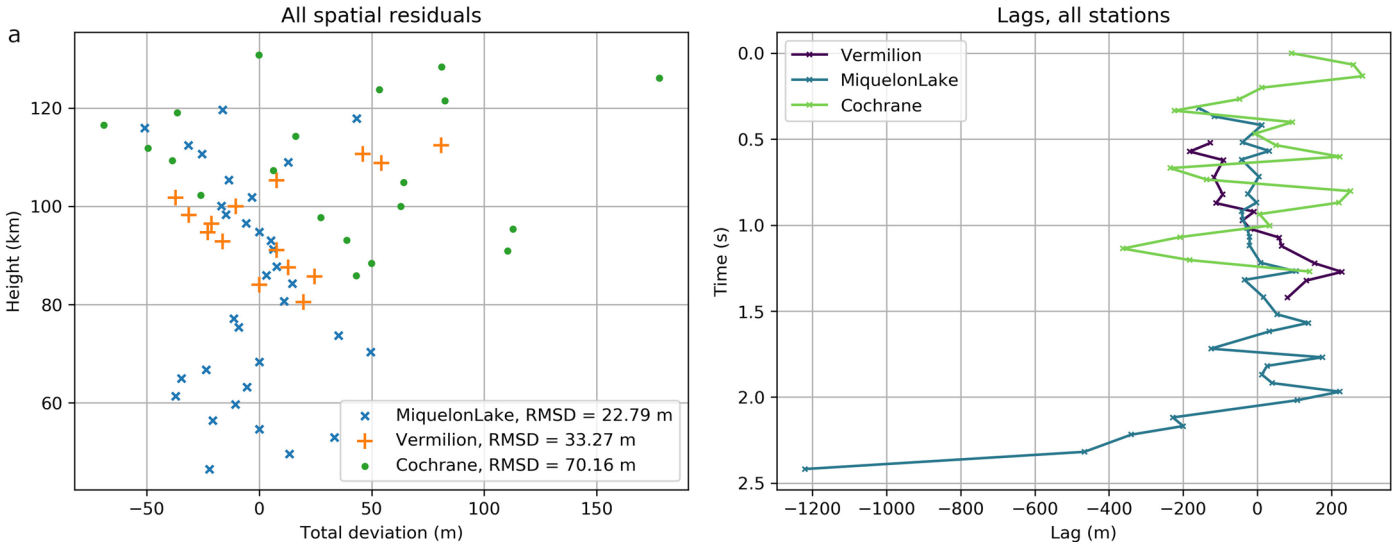

Extended Data Fig. 6 | Trajectory fit errors and dynamics. a) Spatial trajectory fit residuals versus height. b) The observed lag (the distance that the meteoroid falls behind an object with a constant velocity that is equal to the initial meteoroid velocity).

https://doi.org/10.1038/s41550-022-01844-3

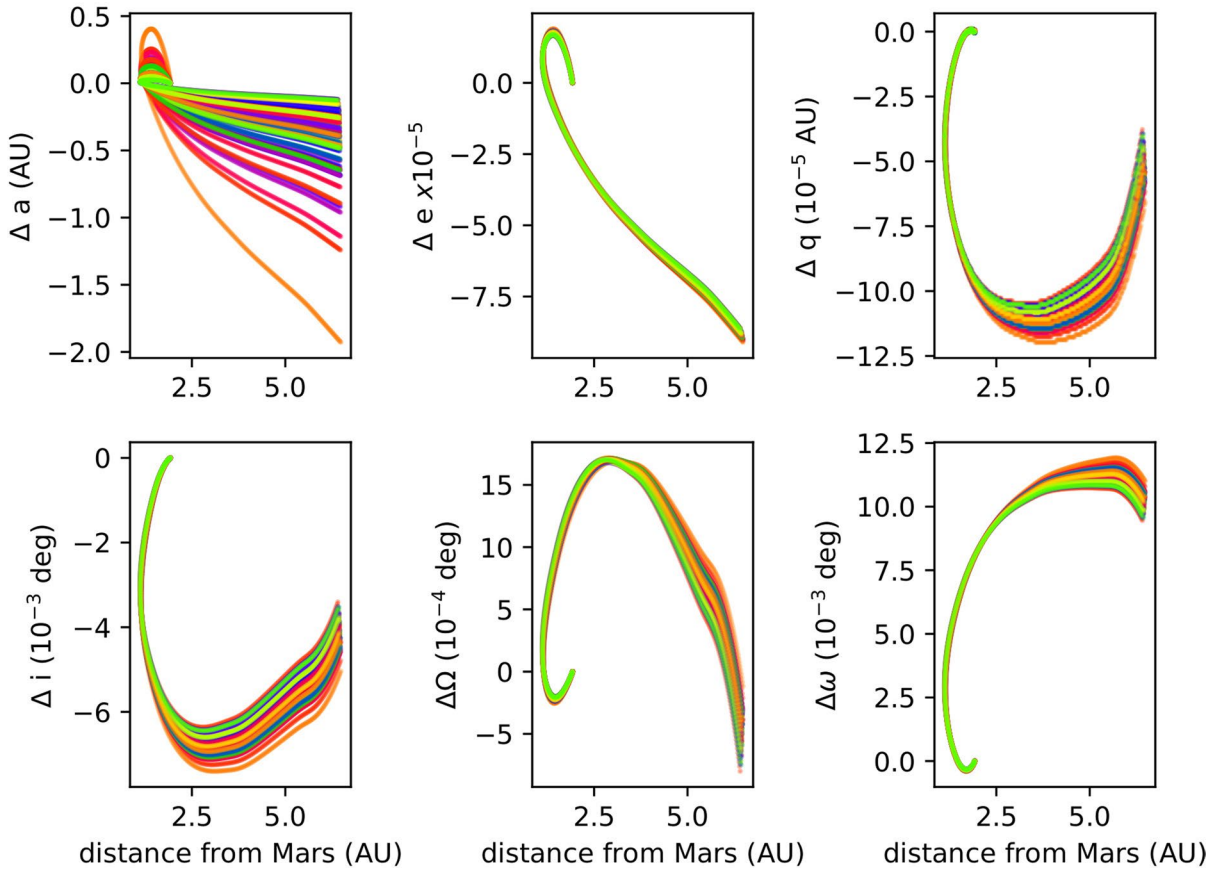

Extended Data Fig. 7 | Change in orbital elements between 60 and 365 days before impact. Each clone is colour-coded individually and represents one sample within the orbital covariance matrix. Time is not shown on any axis, but the clones that start at t - 60 days are clustered at zero and spread out as we go further back in time, as the distance from Mars decreases and then increases again.

https://doi.org/10.1038/s41550-022-01844-3

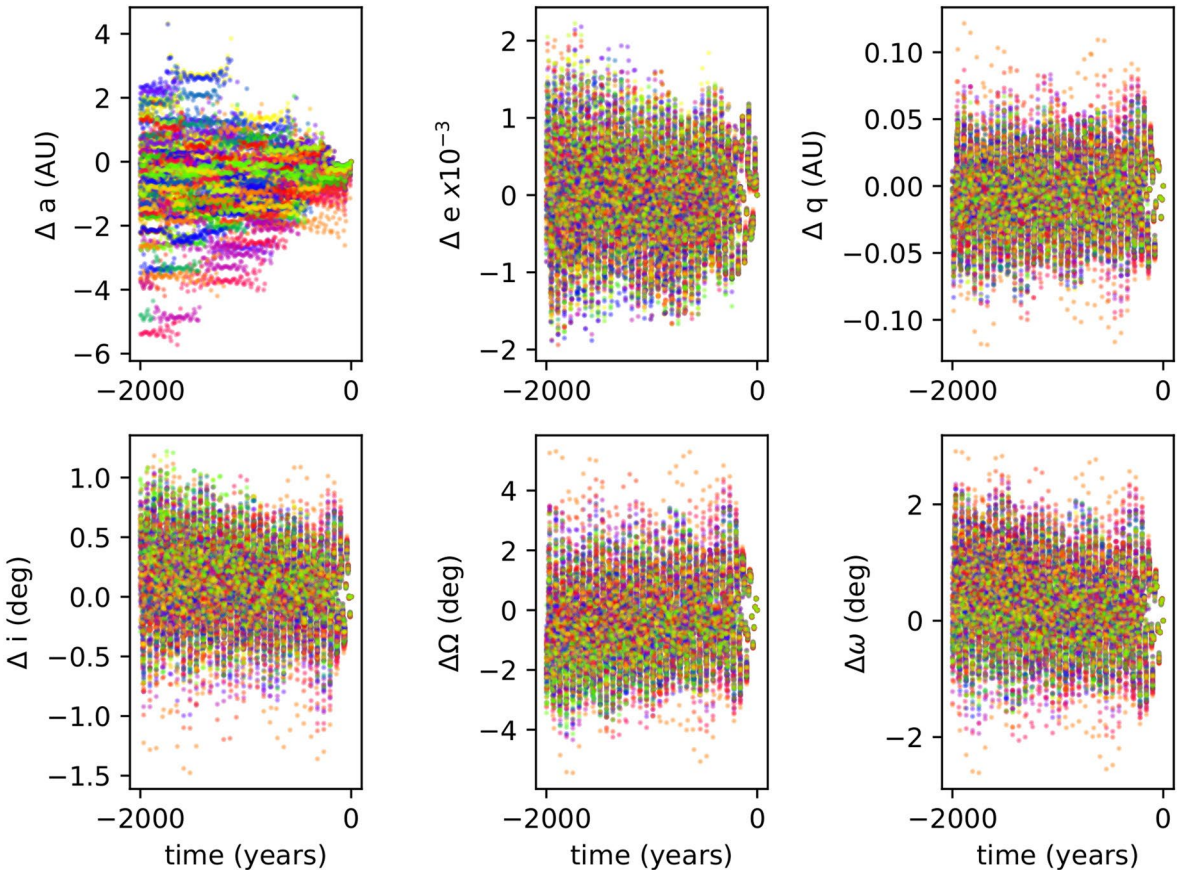

Extended Data Fig. 8 | Change in orbital elements over the last 2000 years. Backwards integration with all planets included. Each clone is colour-coded individually. Planetary perturbations produce small nearly-stochastic changes in the orbital elements.

https://doi.org/10.1038/s41550-022-01844-3

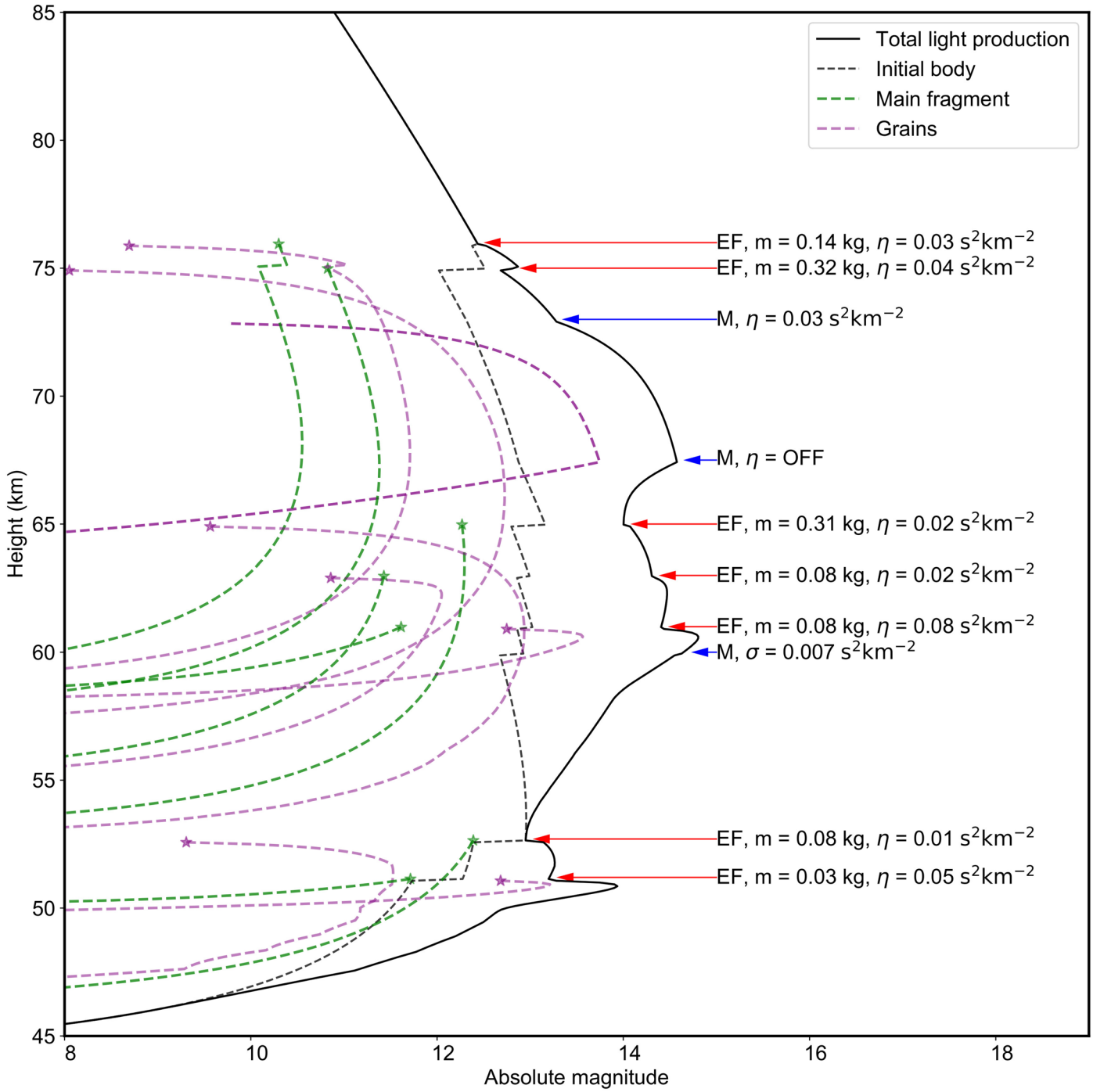

Extended Data Fig. 9 | Details of the modelled individual fragmentations of the meteoroid marked on the simulated light curve. Solid black line is the total light production, the dashed black line is the magnitude of the main body from which fragments are released, green dashed lines are magnitudes of the eroding fragments, and purple lines are magnitudes of the grains ejected either from the main body or the eroding fragments. Arrows indicate where the fragmentations occurred with which parameters, and stars indicate the beginning of individual fragment/grain light curves.

https://doi.org/10.1038/s41550-022-01844-3

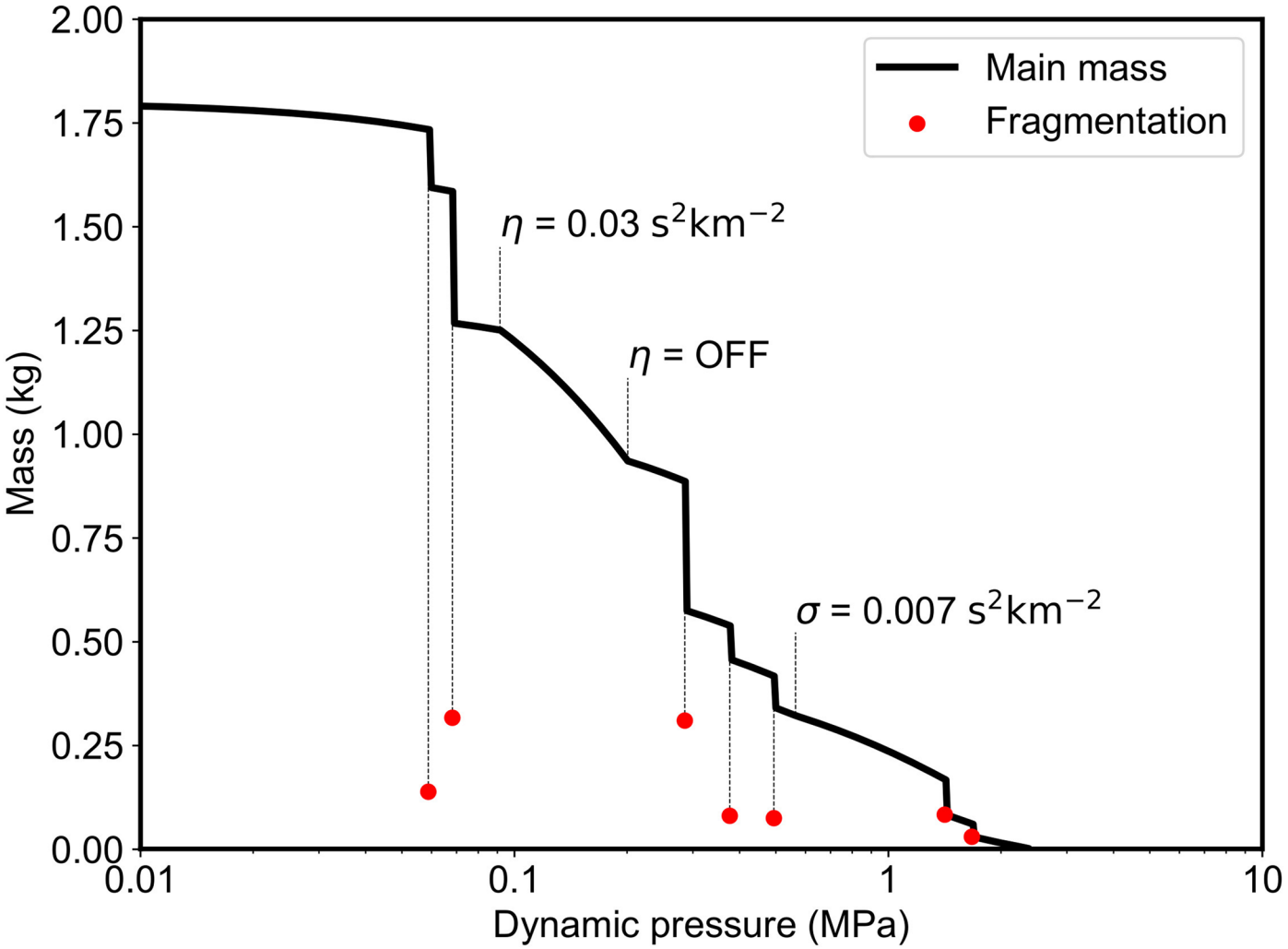

Extended Data Fig. 10 | Modelled mass loss as a function of increasing dynamic pressure. Model fragmentation points and masses of major fragments are marked with red circles. η marks the change in the erosion coefficient, and σ the change in the ablation coefficient of the main body.